Research Square

Preprints are preliminary reports that have not undergone peer review.
They should not be considered conclusive, used to inform clinical practice,
or referenced by the media as validated information.

A systemically delivered X-ray-triggered nanovesicle platform for in situ activation of endogenous neural stem cells and brain circuit repair

Yang Tian

ytian@chem.ecnu.edu.cn

East China Normal University https://orcid.org/0000-0001-8850-0349

Yifan Da

East China Normal University

Xiaohui Li

Fudan University

Mingwei Guo

East China Normal University

Ziyu Li

East China Normal University

Yuandong Liu

East China Normal University

Jing Sun

East China Normal University https://orcid.org/0000-0003-0114-2206

Jingjing Wan

East China Normal University https://orcid.org/0000-0001-9324-2647

Qiangqiang Zhang

Yangtze Delta Region Institute of Tsinghua University

Yudan Chi

Fudan University https://orcid.org/0000-0002-4566-3305

Xinran Ma

East China Normal University

Article

Keywords:

Posted Date: August 4th, 2026

DOI: https://doi.org/10.21203/rs.3.rs-10499445/v1

License: This work is licensed under a Creative Commons Attribution 4.0 International License.
Read Full License

Additional Declarations: There is **NO** Competing Interest.

A systemically delivered X-ray-triggered nanovesicle platform for in situ activation of endogenous neural stem cells and brain circuit repair

Yifan Da[1,†], Xiaohui Li[2,5,†], Ziyu Li[1], Mingwei Guo[3], Yuandong Liu[1], Jing Sun[1], Jingjing Wan[1], Qiangqiang Zhang[6,7], Xinran Ma[3*], Yudan Chi[2,5*], Yang Tian[1,4*]

[1]Department of Chemistry, School of Chemistry and Molecular Engineering, East China Normal University. Shanghai, 200241, China.

[2]Department of Neurosurgery, Huashan Hospital, State Key Laboratory of Medical Neurobiology, MOE Frontiers Center for Brain Science, Fudan University; Shanghai, 200032, China.

[3]Shanghai Key Laboratory of Regulatory Biology, Institute of Biomedical Sciences, School of Life Sciences, East China Normal University, Shanghai 200241, China

[4]Institute of Magnetic Resonance and Molecular Imaging in Medicine, East China Normal University; Shanghai, 200241, China

[5]Institute for Translational Brain Research, MOE Innovative Center for New Drug Development of Immune Inflammatory Diseases, Fudan University; Shanghai, 200032, China.

[6]Advanced Model Animal Research Center, Department of Biotechnology and Biomedicine, Yangtze Delta Region Institute of Tsinghua University; Zhejiang, 314006, China.

[7]Zhejiang Key Laboratory of Multiomics and Molecular Enzymology, Yangtze Delta Region Institute of Tsinghua University; Zhejiang, 314006, China.

† These authors contributed equally: Yifan Da, Xiaohui Li.

*Corresponding authors: xrma@bio.ecnu.edu.cn (X.M), chiy@fudan.edu.cn (Y.C), ytian@chem.ecnu.edu.cn (Y.T)

Abstract

Materials capable of non-invasively accessing deep brain tissues, responding to external stimuli with spatiotemporal precision, and initiating endogenous repair processes remain a notable gap in the treatment of brain injury. Here we engineer XSingletO, a systemically administered nanovesicle platform that integrates blood–brain barrier transport, neural stem cell (NSC)-niche targeting, matrix-metalloproteinase-2 (MMP-2)-responsive payload release, X-ray-triggered singlet-oxygen ($^1O_2$) generation, and ratiometric signal reporting within a single material system. Upon external X-ray irradiation, XSingletO generates a localized $^1O_2$ pulse within native NSC niches, activating resident NSCs and biasing their differentiation toward glutamatergic neurons. In a controlled cortical-impact traumatic brain injury model the resulting newborn neurons migrate over millimetre-scale distances along defined anatomical routes to repopulate cortical lesions, form synaptic connections with host neurons, establish long-range axonal projections, and improve motor behaviours. Integrated single-nucleus RNA sequencing, spatial transcriptomics and proteomics identify a PPARγ-associated programme, and NSC-enriched *Pparg* deletion establishes PPARγ as a required mediator of the early neurogenic response. By combining systemic delivery, remote spatiotemporal control and built-in dose reporting, XSingletO establishes a materials-based strategy for transplantation-free, non-invasive structural and functional regeneration of the injured brain.

Main

Materials that can non-invasively access deep tissues, respond to external stimuli with spatiotemporal precision, and initiate endogenous repair processes are lacking for brain injury[1-5]. Current regenerative strategies for central nervous system damage predominantly rely on supplying exogenous neurotrophic factors or transplanting stem cells expanded and differentiated in vitro[6-14]. However, these approaches face fundamental material-related limitations: neurotrophic factors suffer from short half-lives and poor tissue retention, whereas stem cell transplantation requires invasive delivery and is constrained by poor graft survival and integration, immune rejection and tumorigenic risk[6,10,11]. Alternative strategies that recruit endogenous cells, such as direct glia-to-neuron reprogramming or optogenetic activation of NSCs, reduce the need for donor-cell transplantation but depend on genetic manipulation or

implanted optical hardware, raising concerns regarding long-term safety and secondary tissue injury[15-18]. Reactive oxygen species act as physiological signalling intermediates[19-23], and mitochondrial/redox state can influence stem-cell fate and neurogenesis[24-27]. However, their in vivo application is limited by the lack of methods for spatiotemporally controlled generation and for directing differentiation toward defined neuronal lineages capable of structural repair after brain injury. These limitations collectively point to a materials design challenge: can a single system be engineered to cross the blood–brain barrier, localize to NSC niches, generate a spatially confined chemical cue on demand, and report the delivered signal, all without introducing cells, genes or implanted devices?

Here we report XSingletO, a systemically administered nanovesicle platform that addresses this challenge through integrated material design. The system combines four functional modules within a single vesicle: blood–brain barrier-penetrating angiopep-2 peptides for systemic delivery to the brain; NSC-targeting NFL-TBS peptides for enrichment in the subventricular and subgranular zones[28-32]; an MMP-2-responsive gelatin matrix for environmentally triggered payload release within the NSC niche; and an X-ray-activated organic scintillator (ITC) that generates $^1O_2$ upon external irradiation, co-encapsulated with a ratiometric chemiluminescent probe (RatioCL) for in situ dose reporting. This molecular integration enables a defined treatment cascade: following intravenous administration, XSingletO crosses the blood–brain barrier, accumulates in NSC niches, releases its payload in response to local MMP-2 activity, and, upon external X-ray exposure, produces a controlled $^1O_2$ pulse that is simultaneously monitored ratiometrically. The material platform therefore serves as the primary intervention, converting externally delivered energy into a locally confined chemical signal that activates resident NSCs without the need for cell transplantation, genetic modification or implanted hardware.

We validate this materials-enabled strategy in a controlled cortical-impact traumatic brain injury model. XSingletO-mediated $^1O_2$ stimulation increased NSC proliferation and biased differentiation toward glutamatergic neurons. Lineage tracing showed that subventricular-zone-derived newborn cells migrated over millimetre-scale distances along defined anatomical routes to repopulate cortical lesions, matured within appropriate layers and established synaptic

connections with host neurons. Electrophysiological recordings, retrograde tracing and local-field-potential measurements demonstrated circuit-level integration and network recovery, accompanied by improvements in motor behaviour. Integrated single-nucleus RNA sequencing, spatial transcriptomics and proteomics identified a PPARγ-associated programme, and localized *Pparg* loss of function established PPARγ as a required mediator of the early neurogenic response. Together, these findings establish XSingletO as a materials platform for transplantation-free, non-invasive structural and functional regeneration of the injured brain, and provide a design framework for integrating sequential targeting, environmentally responsive release and remote triggering in tissue-regeneration applications.

Results

Design and characterization of XSingletO as an integrated X-ray-triggered singlet-oxygen nanovesicle system

The XSingletO nanovesicles were constructed based on X-ray-activated chemiluminescent scaffold via modular assembly (**Fig. 1a**). An organic phosphorescent scintillator ITC that produces $^1O_2$ upon X-ray irradiation was synthesized as previously reported (**Supplementary Fig. 1**)[33]. A near-infrared chemiluminescent $^1O_2$ recognition probe, the adamantyl-styryl-chromenone derivative (CTAD) (**Supplementary Fig. 5**), along with a reference dye, Cyanine7 (Cy7), to accurately quantify $^1O_2$ concentration and localization, were synthesized to form the RatioCL probe. All compounds were characterized by nuclear magnetic resonance (NMR) spectroscopy and high-resolution mass spectrometry (HR-MS) (**Supplementary Figs. 2-4 and 6-17**). Gelatin-based peptide precursors were engineered with matrix metalloproteinase-2 (MMP-2)-cleavable GPLGVC linkers, leveraging matrix-metalloproteinase activity associated with activated neurovascular and neural-progenitor microenvironments[34] and the established use of gelatin-based, cell-responsive matrices[35]. Through emulsion cross-linking, ITC and the RatioCL probe were co-encapsulated within these MMP-2-responsive peptide matrices (**Extended Data Fig. 1a**), yielding nanovesicle precursors that specifically recognize and respond to elevated MMP-2 activity in NSC microenvironments (**Extended Data Fig. 1b-e**). Enzymatic hydrolysis of the GPLGVC

sequences subsequently triggered spatially controlled payload release[36]. To effectively target NSC-rich regions within the SVZ and SGZ regions, the precursor was further functionalized with the BBB-penetrating peptide angiopep-2 (ANG) and the NSC-targeting peptide NFL-TBS[37-41], resulting in XSingletO nanovesicles. Transmission electron microscopy (TEM) and dynamic light scattering (DLS) analyses demonstrated that XSingletO possesses a monodisperse nanostructure with an average hydrodynamic diameter of 80.2 ± 4.7 nm (**Fig. 1b**). The successful modular assembly was further confirmed by Fourier-transform infrared spectroscopy (FTIR) (**Extended Data Fig. 2a**).

We first quantified the released $^1O_2$ from MMP-2-cleaved XSingletO nanovesicles utilizing the RatioCL probe. Quantitative analysis using an extracellular $^1O_2$ trapping agent Singlet Oxygen Sensor Green (SOSG) revealed a linear correlation between X-ray dose rate (1-1000 mGy s^{-1}) and ROS concentration (**Fig. 1c and Extended Data Fig. 2f**). To monitor $^1O_2$ levels in situ, we used the RatioCL probe, which underwent a $^1O_2$-specific cycloaddition reaction, yielding distinct near-infrared emission peaks at 720 nm (CTAD-$^1O_2$ adduct) and 773 nm (Cy7 reference signal) (**Fig. 1d**). Notably, the ratiometric signal (F_{720}/F_{773}) exhibited a linear dependence on $^1O_2$ concentration over a physiologically relevant ranges (from 0.03 ± 0.01 to 7.32 ± 1.72 μM, R^2 = 0.992), enabling precise real-time quantification of $^1O_2$ generation (**Extended Data Fig. 2g**). Independent EPR and environmental controls further supported the specificity and robustness of $^1O_2$ detection (**Extended Data Fig. 1d-h**).

Critical to its translational potential, XSingletO demonstrated efficient BBB penetration, with 2.7-fold higher transendothelial transport than non-targeted nanoparticles in an in vitro BBB model (**Fig. 1e**). In vivo, BBB-penetrating peptide functionalization enabled rapid brain accumulation, peaking at 12 h post-injection (**Extended Data Fig. 3a,b**). This enhanced permeability is attributed to its surface functionalization with ANG peptides, which can engage low-density lipoprotein receptor-related protein-1 (LRP1) on brain endothelial cells[37]. In vivo NSC targeting was confirmed by immunofluorescence analysis of brain sections from intravenously injected mice, showing strong colocalization of XSingletO with $Sox2^+$ NSCs in the SVZ and SGZ

(Pearson's coefficients: 0.804 ± 0.031 and 0.812 ± 0.025, respectively; **Fig. 1f,g**). Together, these data establish the material functions required for the treatment sequence: systemic blood–brain barrier transport, localization to adult NSC niches, MMP-2-responsive release and X-ray-controlled, ratiometrically monitored $^1O_2$ generation.

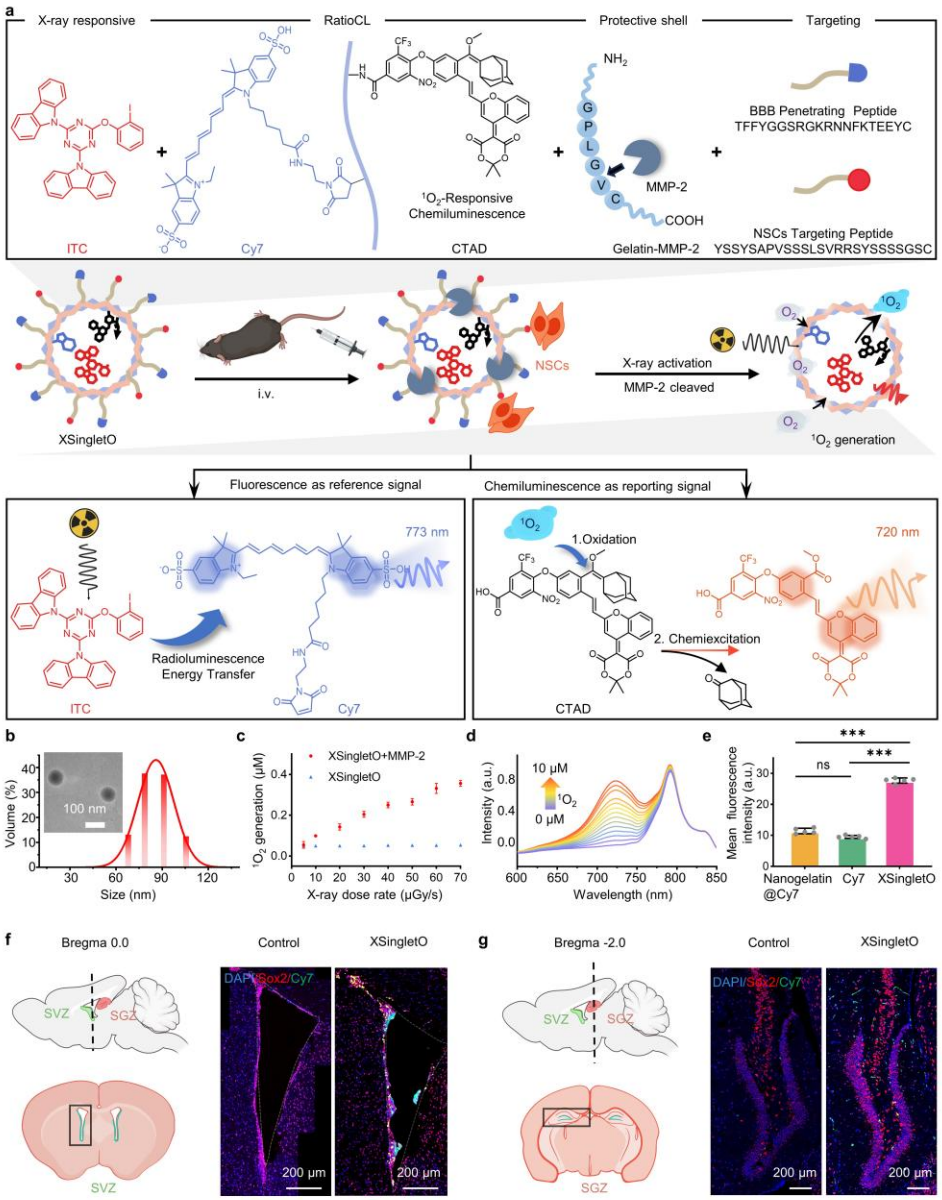


Fig. 1 | Assembly, characterization and brain targeting of XSingletO. a, Schematic of the modular construction, X-ray-triggered $^1O_2$ generation and ratiometric chemiluminescence reporting of XSingletO. **b,** Representative TEM image and DLS size distribution of XSingletO. Scale bar, 100 nm. **c,** $^1O_2$ generation after 10 min of X-ray irradiation at the indicated dose rates.

d, Fluorescence spectra of XSingletO after reaction with $^1O_2$; emission at 720 nm reports the CTAD-$^1O_2$ adduct and emission at 773 nm provides the Cy7 reference. **e,** Permeability of dissociative Cy7, non-targeted nanogelatin vesicles and XSingletO across an in vitro blood–brain barrier Transwell model. Data are mean ± s.d.; dots denote biological replicates (n = 6 per group; each value is the mean of six technical replicates). One-way ANOVA with Tukey's multiple-comparisons test (two-sided); ns, $p \geq 0.05$; ***$p < 0.001$. **f,g,** Coronal brain sections at the SVZ (**f**; bregma 0.0 mm) and SGZ (**g**; bregma -2.0 mm) 12 h after intravenous administration of Cy7-labelled XSingletO or non-targeted vesicles. Sox2, red; Cy7, green; DAPI, blue. Scale bars, 200 μm.

X-ray-controlled singlet-oxygen generation and ratiometric reporting in endogenous NSC niches

To assess the impact of XSingletO nanovesicles on NSC fate, we established a primary culture model using NSCs isolated from adult mouse brains **(Fig. 2a,b**). After a 4-hour incubation with the nanovesicles, X-ray irradiation was applied to generate different concentrations of $^1O_2$ by varying the exposure time, and the optimal dose rate was determined to be 30 μGy s^{-1} (**Extended Data Fig. 2h-j**). EdU incorporation assays showed that 35.0 ± 4.7% of cultured NSCs entered the proliferation phase within 2 d, representing a 2.8-fold increase compared with untreated controls (**Fig. 2c,d**). Concurrently, neuronal differentiation over 7 d yielded 72.0 ± 6.2% βIII-tubulin$^+$ neurons, tripling baseline levels (**Fig. 2e,f**). These findings confirm XSingletO's dual regulation of NSC proliferation and neuronal differentiation. Real-time IVIS tracking of Cy7-labeled XSingletO in C57BL/6 mice showed rapid brain accumulation, peaking at 12 h post-injection (**Extended Data Fig. 3a,b**). Extended X-ray exposure induced no systemic toxicity, with stable body weight, minimal apoptosis, and normal histological and serum profiles (**Extended Data Fig. 3c-f**). These findings confirm efficient BBB penetration and high biocompatibility, providing a pharmacokinetic basis and safety assurance for subsequent neurogenesis studies.

We subsequently investigated the regulation of neurogenesis by XSingletO in two principal NSC niches—Subventricular zone (SVZ) and Subgranular zone (SGZ)—by administering 5 μg kg^{-1} of nanovesicles to C57BL/6 mice, with X-ray activation (30 μGy s^{-1}, 10 min, repeated every three days for three weeks, total dose 126 mGy) at 12 h post-injection. Groups included normal mice (Control), TBI mice (TBI), and treatment cohorts at Week 3, Week 6, Week 9, and Week 15 (**Fig. 2b**). Proliferative NSCs were defined as $BrdU^+/Sox2^+$ double-positive cells, where BrdU incorporation marked actively dividing cells and Sox2 identified the NSC pool[42]. In the SVZ, proliferating NSCs peaked at Week 3 (31.5 ± 3.7 cells per 0.1 mm^2; **Fig. 2g and Extended Data Fig. 4a**). In contrast, SGZ exhibited delayed activation kinetics, with maximal proliferation (18.9 ± 2.8 cells per 0.1 mm^2; **Extended Data Fig. 4b**) emerging at Week 6—a 3-week lag compared to the SVZ. This spatiotemporal disparity suggests region-dependent modulation of NSC activation thresholds, with the SVZ showing faster response kinetics and higher proliferative output compared to the SGZ despite equivalent stimulation.

To verify the differentiation trajectory of proliferating neurons, we conducted dual-label immunofluorescence to detect $BrdU^+/DCX^+$ co-positive cells—a widely used indicator of newly generated immature neurons[42]. In the SVZ at Week 6 (peak phase) (**Fig. 2h and Extended Data Fig. 4c**), 68.2 ± 5.1% of $BrdU^+$ proliferating cells exhibited DCX^+ co-expression, generating 25.3 ± 4.8 dual-positive cells per 0.1 mm^2 (3.8-fold increase versus acute injury TBI group). Conversely, the SGZ showed markedly reduced neurogenic conversion, with merely 14.4 ± 6.3% $BrdU^+$ cells acquiring DCX^+ expression, 4.5-fold lower than the SVZ. These findings demonstrate the SVZ's superior capacity to transform proliferating NSCs into neuronally committed precursors. Neuronal maturation in the SVZ was assessed by MAP2 immunostaining (an established dendritic marker of mature neurons), synaptic density, and dendritic spine density. From Week 3 to Week 9, MAP2 fluorescence increased steadily, reaching 152.3 ± 18.7 arbitrary units (3.8 times the Week 3 level) (**Fig. 2i,j**). Synaptic contacts increased from 0.31 ± 0.07 to 0.9 ± 0.12 synapses $μm^{-1}$, and dendritic spines rose from

208 0.38 ± 0.06 to 1.10 ± 0.14 spines μm^{-1} (**Fig. 2k**). These coordinated enhancements
209 indicate that XSingletO-activated SVZ NSCs adopted a neuronal phenotype and
210 underwent progressive structural and synaptic maturation, ultimately forming neurons
211 capable of participating in functional neural circuits.

212 Lineage-commitment trajectories were resolved by longitudinal flow-cytometric
213 profiling of NSC progeny in the SVZ and SGZ (**Fig. 2l and Extended Data Fig. 4d,e**).
214 Peak conversion was reached at Week 9, when XSingletO drove 70.3 ± 3.2% of the
215 SVZ progeny into the $MAP2^+$ neuronal lineage. By contrast, only 55.4 ± 3.0% of SGZ-
216 derived cells adopted a neuronal fate, indicating a weaker neurogenic output from the
217 SGZ. Consistently, astrocytic differentiation ($GFAP^+$) remained low in the SVZ (17.2
218 ± 3.1%) but was almost one-third higher in the SGZ (22.6 ± 2.8%). The corresponding
219 region-specific lineage distributions are summarized in **Extended Data Fig. 4d,e.**
220 These results demonstrate that while XSingletO reliably biased NSC fate toward
221 neurons in both major adult neurogenic niches, its differentiation-promoting efficacy
222 was markedly stronger in the SVZ than in the SGZ.

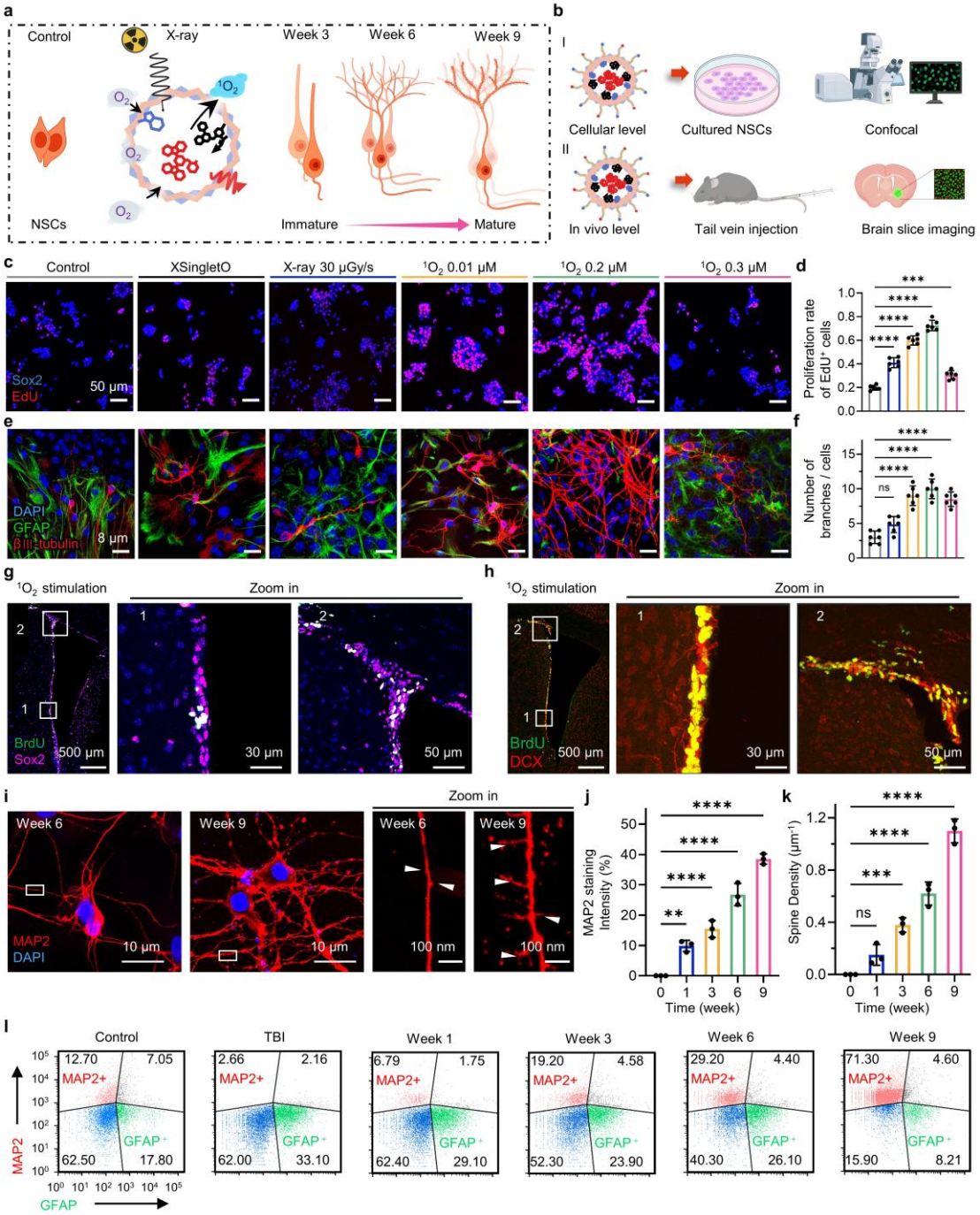


Fig. 2 | XSingletO activates endogenous NSCs and biases neuronal differentiation. a, Treatment and analysis timeline for X-ray-activated XSingletO. **b,** Experimental workflows for cultured NSCs and systemic treatment in mice. **c,** EdU incorporation in cultured NSCs after the indicated XSingletO-generated $^1O_2$ doses; EdU, red; DAPI, blue. Scale bars, 50 μm. **d,** Quantification of EdU$^+$ NSCs. **e,** Neuronal and astrocytic differentiation under the same conditions; βIII-tubulin, red; GFAP, green; DAPI, blue. Scale bars, 8 μm. **f,** Quantification of

neuronal branch number per differentiated NSC. **g,** BrdU and Sox2 immunofluorescence in the SVZ after treatment. Scale bars, 500 μm, 30 μm and 50 μm. **h,** BrdU and DCX immunofluorescence showing newly generated neuroblasts. Scale bars, 500 μm, 30 μm and 50 μm. **i,** $MAP2^+$ neurons at the indicated time points after treatment. Scale bars, 10 μm and 100 nm. **j,k,** Quantification of MAP2 fluorescence intensity (**j**) and dendritic spine density (**k**). **l,** Flow-cytometric analysis of $MAP2^+$ neuronal and $GFAP^+$ astrocytic progeny over time. For d, j and k, data are mean ± s.d. (n = 3 biological replicates per group; each value is the mean of three technical replicates); for f, n = 6 biological replicates per group (each value is the mean of six technical replicates). One-way ANOVA with Tukey's multiple-comparisons test (two-sided); ns, $p \geq 0.05$; ** $p < 0.01$; *** $p < 0.001$; **** $p < 0.0001$. Complete statistical details are provided in the Methods and source data.

XSingletO-activated NSCs regenerate neurons within TBI lesions

We next asked whether this neurogenic capacity translates into structural repair within lesions. To address this question, we established a controlled cortical impact (CCI) model in adult C57BL/6 and Rosa26-LSL-EGFP reporter mice[43]. A 3-mm impactor tip delivered a strike to the right primary motor cortex (M1) at 4.5 m s^{-1}, penetrating 1.8 mm with a 300-ms dwell time, reproducibly removing cortical layers I-V and most of layer VI while sparing the deepest layer VI and underlying white matter. One week before injury, an AAV-SCH9 vector encoding Cre recombinase under the Sox2 promoter was stereotactically injected into the SVZ or SGZ of Rosa26-LSL-EGFP mice, so that EGFP expression permanently labeled NSCs and their progeny. This lineage-tracing strategy allowed direct visualization of newborn cells derived from NSCs that migrated into the peri-lesional cortex after CCI and XSingletO treatment. XSingletO dosing and X-ray activation followed the regimen defined above (see Methods).

Following XSingletO-mediated $^1O_2$ stimulation, $EGFP^+$ newborn cells originating from the SVZ were first detected in the injured cortex at Week 6 and subsequently accumulated along the lesion border and within the regenerated tissue (**Fig. 3a-c and**

Extended Data Fig. 5a). Their density reached to 46.7 ± 2.5 cells per 0.1 mm^2 at Week 9 and continued to increase through Week 15 (**Fig. 3e**), with survival maintained through at least Week 21 (**Extended Data Fig. 5a**). High-magnification images revealed $EGFP^+$ cells with elaborate dendritic trees and spine-bearing processes, suggesting progressive neuronal maturation (**Fig. 3b,c**). Consistently, triple immunostaining at Week 15 showed that many $EGFP^+$ cells within the reconstructed cortex were intermingled with $NeuN^+$ neurons, whereas only smaller subsets overlapped with $Olig2^+$ cells (**Fig. 3d**). Longitudinal lineage quantification further demonstrated a time-dependent shift in $EGFP^+$ NSC-derived progeny, with the $NeuN^+$ fraction gradually increasing from early repair stages to Week 15, accompanied by relative reductions in $Olig2^+$, $GFAP^+$, and marker-negative $EGFP^+$ populations (**Fig. 3f**). These results indicate that XSingletO activation promotes the accumulation and neuronal differentiation of endogenous NSC-derived progeny within the lesion. We next asked whether these newborn neurons acquired excitatory neurotransmitter identities. Immunostaining showed that the majority of $EGFP^+$ neurons co-expressed VGluT1 (73.2 ± 5.1%), with smaller subsets positive for GAD67 or TH (**Supplementary Fig. 18**), supporting a predominantly glutamatergic/excitatory identity among $EGFP^+$ newborn neurons.

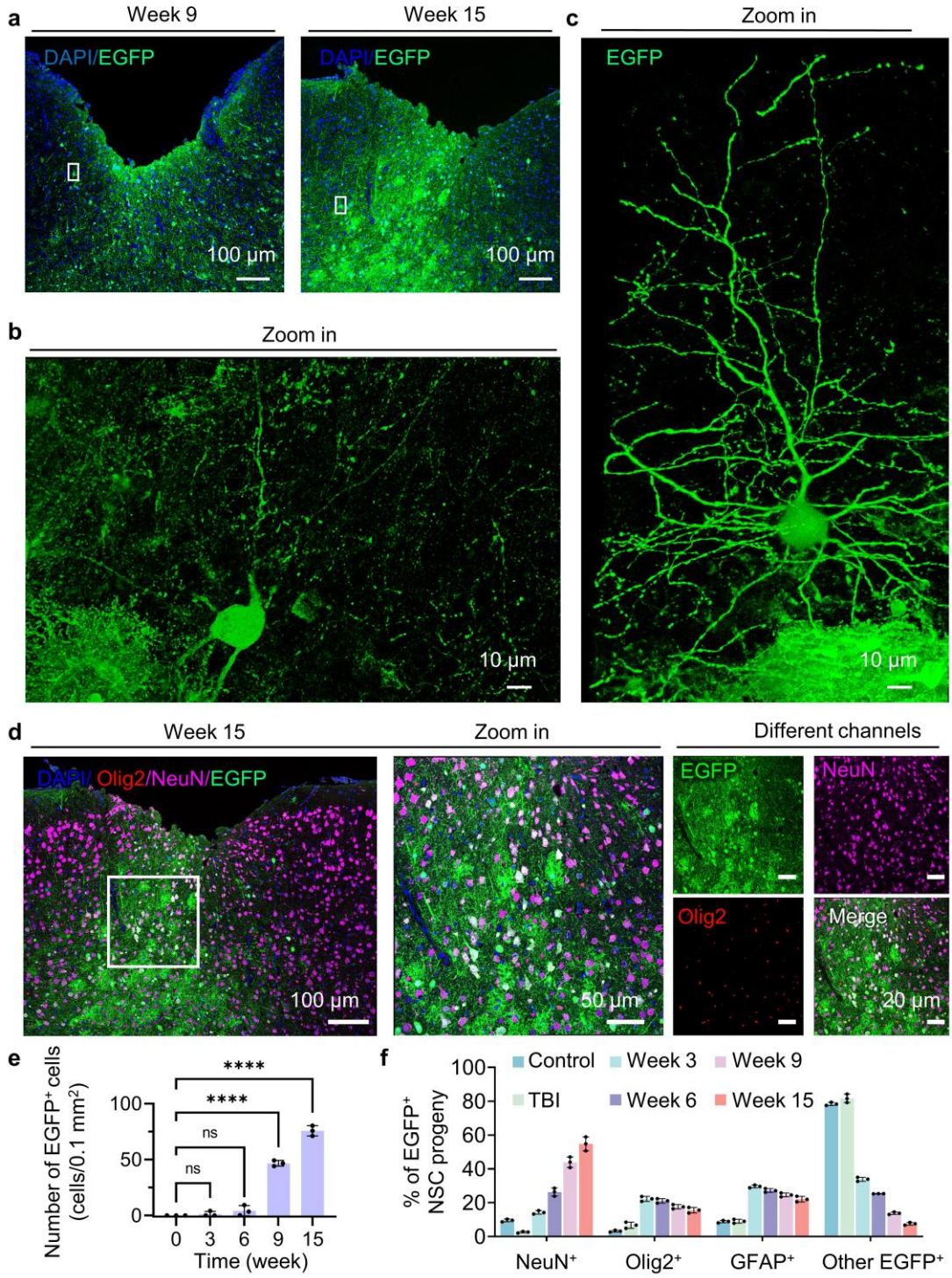


Fig. 3 | XSingletO-activated NSCs regenerate cortical neurons within TBI lesions. a, In situ differentiation of lineage-traced NSCs in the injured cortex. EGFP$^+$ newborn cells (green) derived from SVZ NSCs (AAV-Sox2-Cre in Rosa26-LSL-EGFP mice) appear at the lesion border at Weeks 9 and 15 after XSingletO treatment. Scale bar, 100 μm. **b, c,** Morphological maturation of newborn neurons. Three-dimensional reconstructions of EGFP$^+$ dendritic arbors

at Week 9 (**b**) and Week 15 (**c**). Scale bars, 10 μm; Z-stack depth, 120 μm. **d,** Cell-type distribution within the repaired lesion at Week 15. Triple immunofluorescence for NeuN (magenta, neurons), GFAP (cyan, astrocytes), and Olig2 (red, oligodendrocytes). Scale bars, 100 μm, 50 μm, and 20 μm. **e,** Temporal persistence of newborn neurons. Quantification of $EGFP^+$ cells per 0.1 mm^2 in the lesion area from Week 0 to Week 15. Data are mean ± s.d. (n = 3 biologically independent mice per time point). One-way ANOVA with Tukey's test; ns, $p \geq 0.05$; ****$p < 0.0001$. **f,** Lineage commitment of SVZ-derived NSC progeny over time. Grouped bar plot showing percentages of $NeuN^+$ neurons, $Olig2^+$ oligodendrocytes, and $GFAP^+$ astrocytes. Data are mean ± s.d. (n = 3 biologically independent mice per time point).

SVZ-derived newborn neurons migrate along defined routes to repopulate appropriate cortical layers

Having shown that XSingletO-activated NSCs generate newborn neurons within TBI lesions, we next asked where these cells are positioned within the rebuilt cortex and how they reach the injury site. Correct laminar allocation is essential for re-establishing the input–output architecture of cortical circuits; misplaced neurons, even if abundant, are unlikely to support normal information flow.

Layer-specific analyses revealed that NSC-derived neurons do not accumulate randomly but progressively occupy appropriate cortical laminae. At Week 9 after XSingletO treatment, most $EGFP^+$ cells in the repaired M1 region co-localized with $Ctip2^+$ layer 5/6 excitatory neurons and were concentrated in deep layers immediately subjacent to the cavity (**Fig. 4a-c**). Quantification across layers showed that the majority of labeled cells were L5/6-predominant, with only minor fractions residing in superficial layers (**Fig. 4b**). By Week 15, the distribution shifted: $EGFP^+$ cells were now prominently detected in $Cux1^+$ layers 2/3 while their proportion in $Ctip2^+$ layers 5/6 declined (**Fig. 4b,d**). This transition from a deep layer–predominant to a superficial layer–enriched pattern, summarized schematically in **Fig. 4e**, suggests a progressive shift from deeper to more superficial cortical layers as repair progresses. Importantly, such robust laminar incorporation of lineage-traced neurons was absent in control

groups lacking $^1O_2$ activation, in which the lesion border remained largely devoid of $EGFP^+$ cells.

To determine the origin and migratory routes of these cortical newborn neurons, we used an AAV-SCH9-Sox2-Cre–based lineage-tracing strategy to label NSCs and their progeny in the SVZ and SGZ. Following XSingletO-mediated $^1O_2$ stimulation, $EGFP^+$ NSCs and early progeny remained confined to the SVZ and SGZ niches for the first three weeks. Thereafter, SVZ-derived cells exhibited striking directional migration toward the M1 injury site (**Fig. 4f and Extended Data Fig. 5a**). Migration distances were quantified as the shortest geometric path from the SVZ boundary to the leading front of $EGFP^+$ cells in serial coronal sections, following established methods for neuronal migration analysis[44,45]. The migration front reached 1.22 ± 0.27 mm by Week 6 and a maximum of 1.71 ± 0.62 mm by Week 15, with cells traversing the caudate–putamen (CPu) and corpus callosum (CC) before entering the lesioned cortex, and with no evidence of ectopic dispersal into non-lesioned regions. In contrast, SGZ-derived cells displayed only local dispersion around the dentate gyrus and failed to reach the M1 cortex within the same interval, consistent with their weaker activation and higher fraction of undifferentiated cells (**Extended Data Fig. 5b**).

Together, these results indicate that XSingletO-activated newborn neurons originate mainly from SVZ NSCs, follow a well-defined anatomical route to the traumatic cortical lesion, and ultimately populate the appropriate cortical layers. This combination of long-range reach, laminar precision and absence of ectopic migration underscores the spatial specificity and biosafety of the endogenous regeneration process and sets the stage for testing whether these newly incorporated neurons functionally engage long-range circuits.

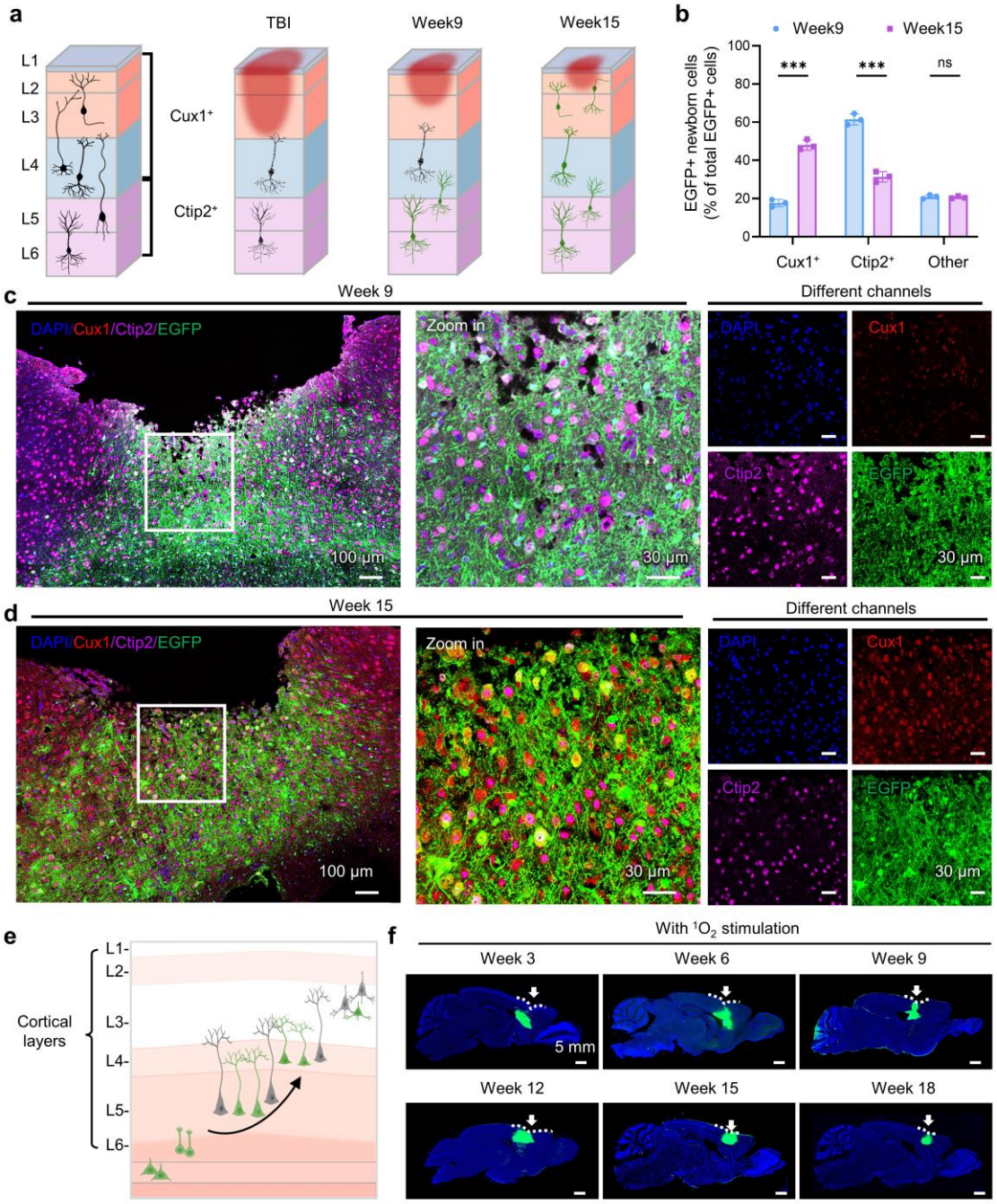


Fig. 4 | Directed migration of SVZ-derived neurons supports layer-specific reconstruction of injured cortex. a, Schematic of cortical layers I–VI with layer-specific markers: Cux1 for layers II/III, Ctip2 for layers V/VI. **b,** Quantification of EGFP$^+$ newborn-cell distribution across Cux1$^+$ superficial, Ctip2$^+$ deep, and Cux1$^-$/Ctip2$^-$ other cortical domains at Weeks 9 and 15. **c,** Deep-layer integration at Week 9. EGFP$^+$ cells (green) co-localize with Ctip2$^+$ cells (cyan) in layers V/VI. Scale bars, 100 μm, 30 μm, and 30 μm. **d,** Superficial-layer integration at Week 15. EGFP$^+$ cells co-localize with Cux1$^+$ cells (red) in layers II/III. Scale bars as in (**c**). **e,**

Schematic summary of progressive laminar redistribution of $EGFP^+$ newborn neurons from deep to superficial cortical layers. **f,** Long-range migration of SVZ-derived cells. Representative coronal brain sections showing $EGFP^+$ cells (green) extending from the SVZ toward the injured cortical region after $^1O_2$ stimulation. White arrows indicate the direction of SVZ-to-lesion migration. Scale bar, 5 mm. Quantitative data in Fig. 4 are presented as mean ± s.d. from n = 3 biologically independent mice per time point; layer distribution and migration-distance analyses were evaluated by one-way ANOVA with Tukey's multiple-comparisons test; ns, $p \geq 0.05$; ***$p < 0.001$.

Newborn neurons reconstruct neural circuits and restore function

To investigate the functional restoration of neural connectivity, we utilized patch-clamp electrophysiology to assess synaptic connections between newborn neurons and pre-existing neurons in brain slices from TBI mice after 15 weeks of treatment. As illustrated in **Fig. 5a**, an engineered AAV2/sch8-CMV-hChR2(H134R)-mCherry vector was used to express the blue-light-gated channelrhodopsin-2 ChR2(H134R) in host neurons, alongside mCherry for fluorescent labeling. Meanwhile, newly generated neurons migrating from the SVZ to the injured cortex were tagged with the AAV-SCH9-Sox2-Cre vector. Upon 10-ms blue-light stimulation of ChR2-expressing host neurons (**Fig. 5b**), whole-cell recordings from EGFP-labelled newborn neurons showed clear excitatory postsynaptic potentials after each pulse (**Fig. 5c**). These postsynaptic responses were abolished by the AMPA and NMDA receptor antagonists NBQX and CPP[46], respectively (**Fig. 5c,d**). In parallel, recordings from $mCherry^+/ChR2^+$ host neurons showed robust light-evoked currents that persisted in the presence of NBQX and CPP (**Fig. 5c**), confirming that the antagonists blocked glutamatergic synaptic transmission rather than impairing ChR2-mediated optical activation of host neurons. These results demonstrate that newborn neurons form functional synaptic connections with pre-existing host neurons, facilitating integration into repaired cortical networks.

Axonal routing of EGFP-labeled newborn neurons was examined in sagittal sections at Week 15 in the TBI model (**Fig. 5e**). Cell bodies in the injured M1 (box 1) extended

GFP-filled fibers toward subcortical regions, prominently including the thalamic area (box 2). To verify this thalamic projection, the retrograde tracer CTB-AF594 was injected into the thalamus. After 7 days, a subset of EGFP-positive newborn neurons in M1 was co-labeled with CTB-AF594 (**Fig. 5f**), indicating that newborn neurons establish long-range axonal projections from the repaired M1 to the thalamus, supporting circuit reconstruction beyond the local lesion.

Electrophysiological network reorganization was assessed by recording local field potentials (LFPs) within the lesioned area across multiple groups, including healthy control mice (Control), acute injury mice (TBI), and treatment cohorts at Week 3, Week 6, Week 9, and Week 15 (**Fig. 5g**). Delta band power (δ, 1-4 Hz) initially increased, due to the loss of inhibitory interneurons; however, it subsequently declined, indicating effective modulation of glutamatergic hyperexcitability. In contrast, beta/low-gamma band power (20-50 Hz), which reflects excitatory synaptic efficacy, showed gradual recovery, reaching near baseline levels by Week 15. Nonlinear analysis of LFP signals demonstrated a significant reduction in multiscale sample entropy post-injury, followed by a linear recovery, suggesting enhanced computational capacity of the neural network through improved synaptic integration.

Behavioral recovery was quantified using rotarod, voluntary wheel running, and T-maze alternation tests in experimental groups consistent with those used for LFP recordings (**Fig. 5h-j**). Acute-injury TBI mice showed severe motor and cognitive deficits: rotarod latency and running distance dropped to 35% and 28% of control values, respectively, while maze decision time increased 2.7-fold with only 32% accuracy. By Week 3, rotarod latency and running activity showed partial recovery, whereas T-maze performance remained close to chance level, and by Week 15 the animals exhibited substantial functional recovery, with behavioral performance approaching that of control mice across the tested tasks. These results indicate that targeted $^1O_2$ delivery effectively reverses injury-induced impairments and supports the restoration of motor coordination, endurance, and spatial working memory, consistent with structural repair and strengthened neural connectivity after TBI.

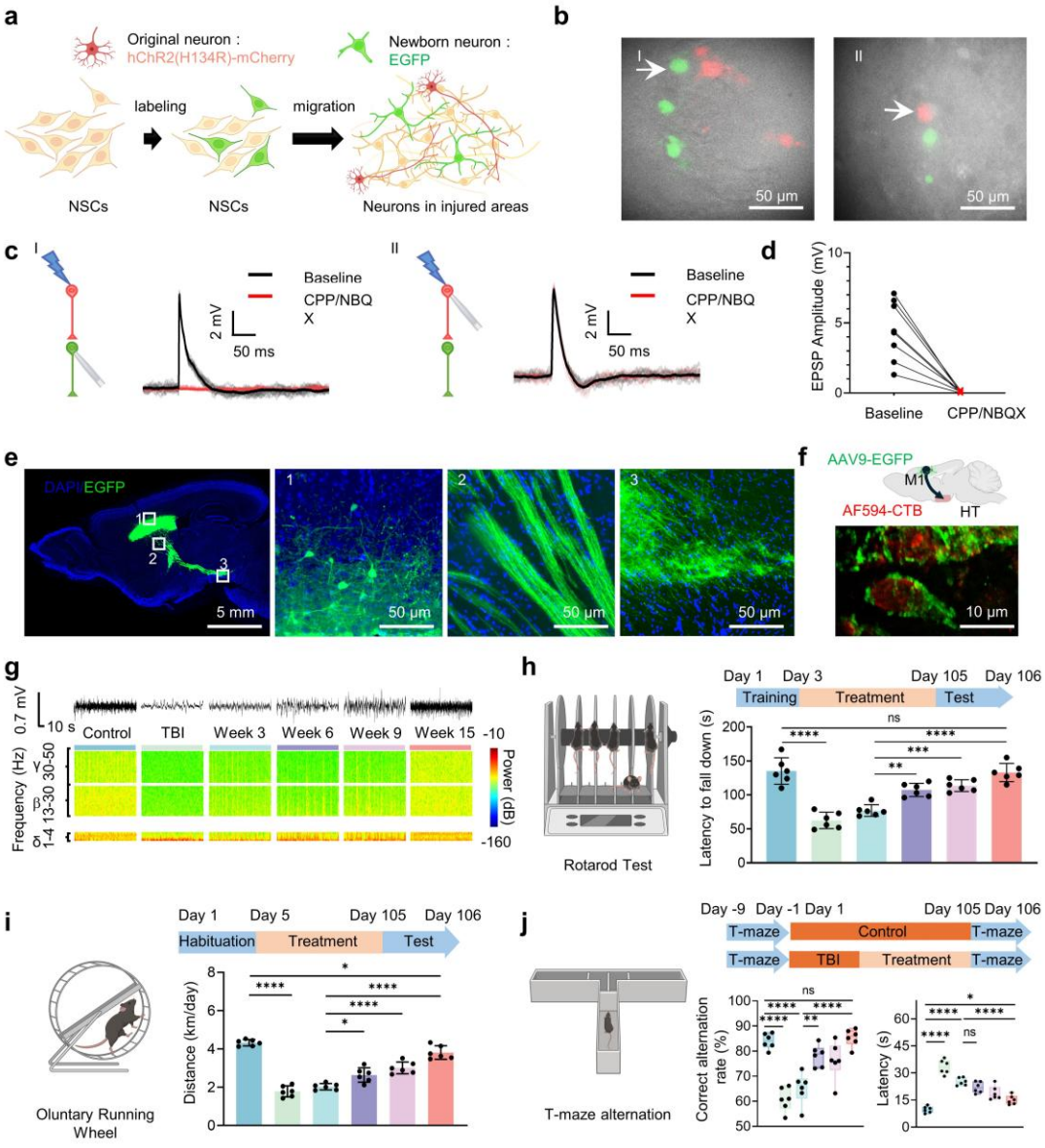


Fig. 5 | Functional reconstruction of neural circuits after XSingletO treatment. a, Experimental design for optogenetic circuit mapping. AAV-ChR2-mCherry was expressed in host neurons, whereas EGFP labelled newborn neurons derived from SVZ NSCs. **b,** Patch-clamp recording configuration in a coronal brain slice at week 15 showing mCherry^{+} host neurons and an EGFP^{+} newborn neuron. Scale bar, 50 μm. **c,** Light-evoked excitatory postsynaptic potentials (EPSPs) recorded in a newborn neuron during blue-light stimulation of ChR2^{+} host neurons. EPSPs were abolished by the AMPA and NMDA receptor antagonists NBQX and CPP. Traces are averages of 20 trials. Scale bars, 2 mV and 50 ms. **d,** Light-evoked EPSP amplitude before and after NBQX/CPP blockade. Cell-level traces are shown with animal-level summary statistics in the source data. **e,** Sagittal section showing EGFP^{+} axons

from the repaired M1 region (box 1) projecting to the thalamus (box 2) and hypothalamus (box 3). Scale bars, 5 mm and 50 μm. **f,** Retrograde tracing from the thalamus with CTB-AF594 identifies $EGFP^+$ newborn neurons in M1. Scale bar, 10 μm. **g,** Local-field-potential power spectra for control, TBI and XSingletO-treated mice at the indicated time points. LFP recordings were analysed from n = 6 mice per group, with one peri-lesional recording site per mouse. **h-j,** Behavioural recovery measured by rotarod latency (**h**), voluntary wheel-running distance (**i**), and T-maze alternation rate and decision latency (**j**). Data are mean ± s.d. (n = 6 mice per group). One-way ANOVA with Tukey's multiple-comparisons test; ns, $p \geq 0.05$; *$p < 0.05$; ** $p < 0.01$; *** $p < 0.001$; **** $p < 0.0001$. Schematic in a created with BioRender.com.

Integrated multi-omics prioritizes a PPARγ-associated programme during XSingletO-mediated repair

To define the cellular states and molecular pathways associated with XSingletO-mediated repair, we integrated single-nucleus RNA sequencing (snRNA-seq), TMT-based quantitative proteomics and spatial transcriptomics across Control, TBI and XSingletO-treated groups at Weeks 3, 9 and 15 (**Fig. 6a**). After quality control, 156,508 nuclei isolated from the SVZ and peri-lesional cortex were retained for analysis. UMAP resolved six major cell populations—neurons, astrocytes, microglial cells, oligodendrocyte precursor cells (OPCs), oligodendrocytes and endothelial cells—whose identities were supported by mutually enriched canonical markers (**Fig. 6b,c and Supplementary Fig. 19**).

Cell-type composition analysis captured the marked neuronal loss induced by TBI and its progressive reversal during repair (**Fig. 6d**). Neuronal abundance declined sharply after injury but increased progressively from Week 3 to Week 15 after XSingletO treatment. Injury-associated changes in astrocytes, microglial cells, OPCs, oligodendrocytes and endothelial cells were also remodelled over the same period. These coordinated shifts indicate that XSingletO-mediated regeneration involves broad reorganization of the local cellular ecosystem rather than selective expansion of a single

lineage.

To resolve neuronal heterogeneity and state transitions, we re-clustered 59,391 neuronal nuclei into seven transcriptionally distinct states, comprising four excitatory-associated subclusters (N1, N2, N6 and N7) and three inhibitory/GABAergic-associated subclusters (N3, N4 and N5) (**Fig. 6e and Supplementary Figs. 20 and 21**). Their relative abundance changed markedly across the injury-to-repair sequence. TBI and the early repair phase were characterized by relative enrichment of transitional or inhibitory-biased states, whereas excitatory-associated populations progressively recovered and became increasingly prominent at later stages, particularly by Week 15 (**Fig. 6f**). This temporal reorganization was consistent with the emergence and maturation of newborn neurons observed by lineage tracing and histological analysis.

We next positioned these neuronal states along a neurogenic continuum using four curated transcriptional programmes: an NSC-related signature comprising *Nes, Sox2, Msi1, Prom1* and *Pax6*; a neurogenesis-related signature comprising *Neurod1, Dcx, Tubb3, Rbfox3* and *Map2*; an NSC proliferation-related signature additionally containing *Mki67* and *Mcm2*; and an early neuronal differentiation-related signature comprising *Dcx, Tubb3* and *Neurod1* (Supplementary Table 1). The NSC-related programme was not uniformly elevated across the neuronal compartment but was concentrated in restricted regions of the neuronal UMAP, principally corresponding to N4, N5 and a subset of N1 (**Fig. 6g**). Consistently, both the NSC-related and NSC proliferation-related scores remained low across most neuronal states, with sparse high-scoring cells most evident in N4 and N5 (**Supplementary Fig. 22**). By contrast, the neurogenesis-related programme was distributed more broadly across the neuronal landscape (**Fig. 6h**), and neurogenesis-related and early differentiation-related scores were preferentially enriched in N7, N1, N2 and N6, consistent with progressive neuronal commitment and maturation (**Supplementary Fig. 22**).

Monocle2[47] analysis further organized the seven neuronal subclusters along a continuous pseudotime trajectory extending from precursor-like or transitional states towards differentiated excitatory-associated neurons (**Fig. 6i and Supplementary Fig.**

23). Together, the changes in subcluster composition, module-score distribution and pseudotime organization support a sequential transition from restricted precursor-associated states to neurogenesis-associated and differentiating neuronal states, rather than uniform induction of an NSC-like programme throughout the neuronal compartment. Pathway-level analyses were consistent with this progression. KEGG enrichment revealed dynamic regulation of glutamatergic synapse, axon guidance, neuroactive ligand-receptor interaction, endocannabinoid signalling and lipid-metabolic pathways, whereas GO analysis showed increasing engagement of synapse assembly, regulation of synapse organization, cell–cell adhesion, axonogenesis and central nervous system projection-neuron programmes during later repair stages (**Supplementary Figs. 24 and 25**). These findings indicate that XSingletO-induced regeneration encompasses not only the emergence of neurogenic neuronal states but also their subsequent maturation and engagement of molecular programmes required for circuit reconstruction. Stage-dependent immunoblotting of PPARγ and related pathway proteins provided additional support for a PPAR-linked response (**Supplementary Fig. 26**).

To determine whether the snRNA-seq-defined states were spatially organized within the injured brain, we mapped the cell populations identified by snRNA-seq onto spatial transcriptomic spots from TBI and XSingletO-treated brain sections collected at Weeks 3, 9 and 15 (**Extended Data Fig. 6a,b** and **Supplementary Fig. 27**). The resulting spatial annotations were consistent with the single-nucleus analysis. In untreated TBI brains, the peri-lesional cortex showed extensive neuronal depletion and was dominated by astrocytic regions, whereas the NSC-related N4 and N5 states remained largely confined to the SVZ. Following XSingletO treatment, neuronal populations progressively reappeared near the lesion at Week 3 and expanded into the reconstructed cortical region at Weeks 9 and 15, accompanied by reorganization of astrocytic and oligodendrocyte-associated domains (**Extended Data Fig. 6c,d**).

Spatial trajectory analysis provided additional anatomical support for the neurogenic continuum inferred from snRNA-seq. In untreated TBI brains, *Dcx* expression and

NSC-related module activity remained restricted to the SVZ. After treatment, *Dcx*-enriched and NSC-related-gene-set-high regions progressively extended from the SVZ towards the peri-lesional cortex: a short arc emerged at the SVZ border at Week 3, lengthened towards the lesion by Week 9 and formed a near-continuous SVZ-to-lesion trajectory by Week 15 (**Extended Data Fig. 6e–h**). Spatial projection of pathway activity further showed transient enrichment of PPAR signalling in the SVZ during the early repair phase, temporally coinciding with endogenous NSC activation (**Supplementary Fig. 28**). Consistently, spatial co-occurrence analysis identified an SVZ-associated niche enriched in the N4 and N5 states that became progressively more prominent during repair (**Extended Data Fig. 6i and Supplementary Fig. 29**). Thus, spatial transcriptomics independently corroborated the snRNA-seq-defined transition from precursor-associated states to differentiating neuronal populations and showed that this process occurred within an anatomically organized, SVZ-linked repair microenvironment rather than as a diffuse response.

To identify molecular pathways converging with these cellular and spatial transitions, we analysed TMT-based proteomic profiles of microdissected SVZ tissue. PPAR signalling was not the highest-ranked pathway at every individual time point, but it was reproducibly enriched in comparisons of Weeks 3, 9 and 15 with TBI, whereas many higher-ranked terms were restricted to a single repair stage (**Fig. 6j**). This recurrence, together with repeated enrichment of fatty-acid degradation, fatty-acid elongation and related lipid-metabolic pathways, nominated PPAR-associated metabolic regulation as a sustained component of the repair response.

We therefore compared the three PPAR-family members across the snRNA-seq datasets. Within neuronal populations exhibiting elevated neurogenesis-related module scores, *Pparg* was detected in a substantially larger fraction of cells than *Ppara* or *Ppard*. Its expression was reduced after TBI and progressively restored during XSingletO-mediated repair (**Fig. 6k**). PPAR-associated lipid-handling genes, including *Apoe, Lpl* and *Abca1*, displayed distinct stage-dependent changes rather than uniform co-induction, indicating broader remodelling of lipid metabolism during regeneration.

Spatial transcriptomics provided an independent anatomical readout. In neuron-annotated regions, both *Pparg* expression and the proportion of *Pparg*-positive spots increased at Weeks 9 and 15 relative to TBI, whereas *Ppara* remained sparsely expressed (**Fig. 6l**). Although *Ppard* also increased during repair, its enrichment was less consistently associated with the neurogenesis-related neuronal populations defined by snRNA-seq. Across the transcriptomic and spatial datasets, *Pparg* therefore showed the most consistent association with the regenerative programme, prioritizing *Pparg* for functional validation without excluding potential contributions from *Ppara* or *Ppard*.

Together, the snRNA-seq, spatial transcriptomic and proteomic datasets link XSingletO-mediated regeneration to a recurrent PPAR-associated metabolic programme and provide a transparent basis for prioritizing *Pparg*. However, transcript abundance, spatial enrichment and pathway-level associations remain correlative and cannot establish receptor activation or functional necessity. We therefore next used localized, NSC-enriched *Pparg* loss of function to determine whether *Pparg* is required for the early neurogenic response to XSingletO-mediated $^1O_2$ stimulation.

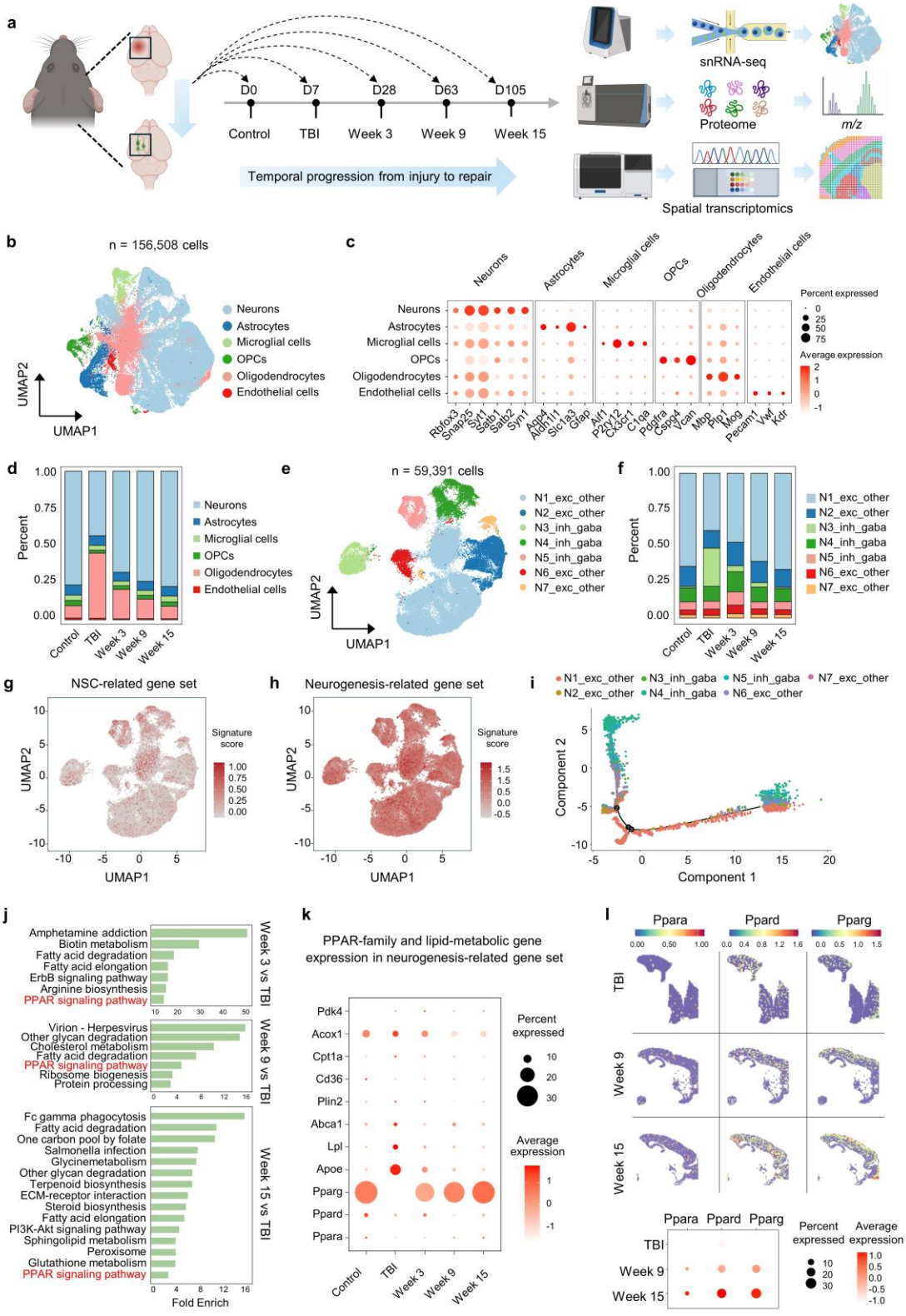


Fig. 6 | Integrated single-nucleus, proteomic and spatial analyses prioritize a PPARγ-associated programme during XSingletO-mediated repair. a, Experimental design for snRNA-seq, TMT-based proteomics and spatial transcriptomics across

Control, TBI and repair stages. **b,** UMAP of 156,508 nuclei annotated as six major brain cell populations. **c,** Canonical marker-gene dot plot validating the major cell-type annotations. **d,** Relative abundance of major cell populations across Control, TBI, Week 3, Week 9 and Week 15. **e,** Re-clustering of 59,391 neuronal nuclei into seven excitatory- or inhibitory-associated subclusters. **f,** Temporal changes in neuronal-subcluster composition. **g,h,** UMAP feature plots of NSC-related (**g**) and neurogenesis-related (**h**) module scores. **i,** Monocle2 pseudotime trajectory of neuronal subclusters. **j,** Proteomic pathway enrichment at Weeks 3, 9 and 15 relative to TBI; PPAR signalling is highlighted in red. **k,** PPAR-family and lipid-metabolic gene expression in neurogenesis-associated neuronal populations; dot size indicates the percentage of expressing cells and colour indicates scaled average expression. **l,** Spatial expression of*Ppara*, *Ppard* and *Pparg* in neuron-annotated tissue regions at TBI, Week 9 and Week 15, with a summary dot plot of percentage expression and scaled average expression.

NSC-enriched *Pparg* deletion establishes PPARγ as a necessary mediator of $^1O_2$-induced neurogenesis

The integrated multi-omics analyses prioritized PPARγ as the PPAR-family member most consistently associated with neurogenesis-related states and repair-region neurons. These data, however, could not distinguish a functional mediator from a secondary marker of NSC activation. We therefore tested whether PPARγ is required for $^1O_2$-induced NSC proliferation and early neuronal commitment in vivo.

To selectively perturb PPARγ in adult neural stem/progenitor cells, we generated a localized conditional loss-of-function strategy in *Pparg*$^{fl/fl}$ mice. AAV-Nestin-Cre-mCherry or control AAV-Nestin-mCherry was stereotactically injected into the SVZ, followed by inactive nanovesicle treatment or XSingletO-mediated $^1O_2$ stimulation. This design yielded four experimental groups: Control, Stimulation, cKO, and cKO + Stimulation (**Fig. 7a**). Specifically, Control mice received AAV-Nestin-mCherry and inactive nanovesicles; Stimulation mice received AAV-Nestin-mCherry and XSingletO-mediated $^1O_2$ stimulation; cKO mice received AAV-Nestin-Cre-mCherry

and inactive nanovesicles; and cKO+Stimulation mice received AAV-Nestin-Cre-mCherry and XSingletO-mediated $^1O_2$ stimulation. Thus, the experiment directly tested whether stimulation-induced NSC activation persists when PPARγ is removed from the targeted Nestin-lineage NSC/NPC population. Genotyping and localized SVZ targeting were independently validated (**Supplementary Fig. 30a,b**).

We first validated the efficiency of conditional *Pparg* deletion in the SVZ. In mice receiving AAV-Nestin-Cre-mCherry, PPARγ immunoreactivity was strongly reduced in virally targeted mCherry$^+$ cells and in Sox2$^+$ NSCs compared with AAV-Nestin-mCherry controls (**Fig. 7b,c**). Quantification of PPARγ fluorescence intensity confirmed efficient depletion of PPARγ in the targeted NSC population. These data establish that the AAV-Nestin-Cre strategy produces localized, NSC-enriched *Pparg* deletion in the SVZ.

We next examined whether $^1O_2$ stimulation activates PPARγ in NSC/NPCs. In PPARγ-intact mice, XSingletO-mediated $^1O_2$ stimulation increased nuclear PPARγ signal in Sox2$^+$ cells within the SVZ compared with control mice (**Fig. 7d**). This nuclear enrichment is consistent with activation of PPARγ signaling in the NSC niche during the onset of the neurogenic response.

We then asked whether PPARγ is required for the proliferative response to $^1O_2$ stimulation. In PPARγ-intact mice, $^1O_2$ stimulation markedly increased the fraction of BrdU$^+$ cells among mCherry$^+$Sox2$^+$ NSCs, indicating robust stimulation-induced proliferation (**Fig. 7e**). By contrast, this increase was largely abolished in AAV-Nestin-Cre-mCherry-injected *Pparg*$^{fl/fl}$ mice, whereas basal BrdU incorporation remained low in both control and cKO groups. Thus, PPARγ is required for the proliferative activation of Nestin-lineage Sox2$^+$ NSCs after $^1O_2$ stimulation.

Finally, we examined whether PPARγ is also required for early neuronal commitment of virally targeted progeny. In PPARγ-intact mice, $^1O_2$ stimulation increased the fraction of BrdU$^+$ cells among mCherry$^+$DCX$^+$ newborn neuroblasts in the SVZ and adjacent early migratory region (**Fig. 7f**). In contrast, NSC-enriched *Pparg* deletion markedly reduced this stimulation-induced BrdU$^+$ fraction among mCherry$^+$DCX$^+$ cells. These findings indicate that PPARγ is not merely associated with the transcriptional transition

observed in the multi-omics data but is functionally required for both NSC proliferative activation and the generation of DCX^+ newborn neuroblasts in response to controlled $^1O_2$ stimulation.

Together, these loss-of-function experiments provide causal evidence that the PPARγ signal identified by multi-omics is required for the early neurogenic response. XSingletO-mediated $^1O_2$ stimulation increased nuclear PPARγ in *Sox2*-positive NSCs, whereas NSC-enriched *Pparg* deletion blocked stimulation-induced proliferation and the generation of DCX-positive newborn neuroblasts. PPARγ therefore acts as a necessary downstream effector linking a transient redox cue to NSC proliferation and early neuronal commitment; its contribution to later migration, maturation and circuit integration remains to be determined. Pharmacological modulation of PPARγ produced concordant changes in DCX, NeuroD1, Tuj1 and GFAP abundance (**Supplementary Fig. 31**).

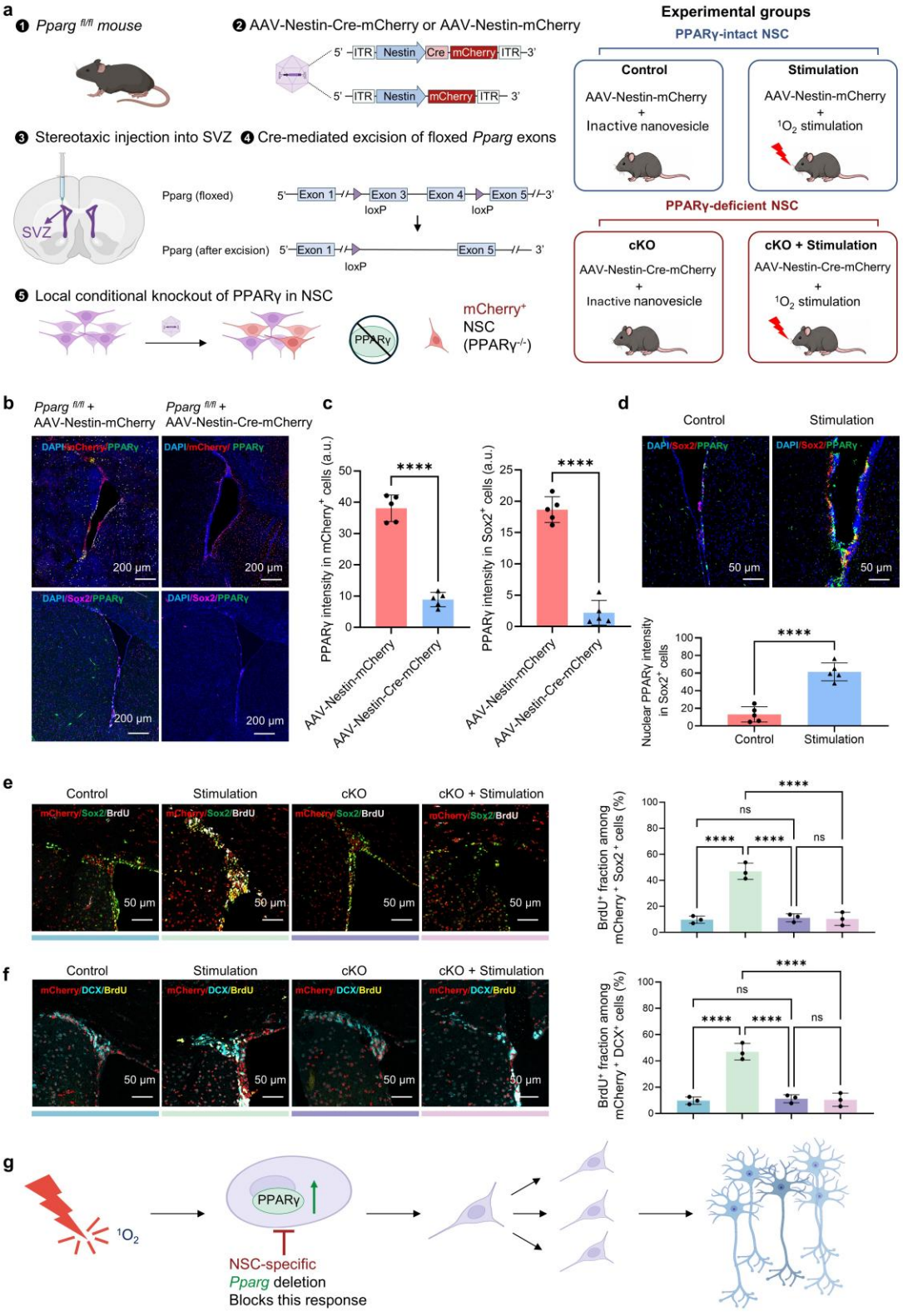


Fig. 7 | NSC-enriched Pparg deletion blocks $^1O_2$-induced NSC proliferation and early neuronal commitment. a, Localized conditional *Pparg* deletion strategy in the SVZ of Ppargfl/fl mice and the four experimental groups: Control, Stimulation, cKO and cKO +

Stimulation. **b,c,** Validation and quantification of PPARγ depletion in virally targeted mCherry-positive cells and *Sox2*-positive NSCs. **d,** Nuclear accumulation of PPARγ in *Sox2*-positive NSCs after $^1O_2$ stimulation. **e,** BrdU incorporation in mCherry-positive/*Sox2*-positive NSCs across the four groups. **f,** Generation of mCherry-positive/BrdU-positive/DCX-positive newborn neuroblasts across the four groups. **g,** Working model in which spatially confined $^1O_2$ activates a PPARγ-dependent early neurogenic response that is blocked by NSC-enriched *Pparg* deletion. Data are mean ± s.d.; each dot represents one biologically independent mouse. Statistical significance was determined by two-tailed unpaired Student's t-test for two-group comparisons or one-way ANOVA with Tukey's multiple-comparisons test for four-group comparisons. ns, not significant; ****$p < 0.0001$. Statistical details are provided in the Methods.

Discussion

The central advance of this work is an integrated material system that replaces ex vivo cell manufacture and intracranial transplantation with externally timed, spatially confined activation of endogenous neural stem cells. XSingletO achieves this through a sequential cascade: systemic administration, blood–brain barrier transport, NSC-niche accumulation, MMP-2-responsive payload release, X-ray-triggered $^1O_2$ generation, and ratiometric reporting of the delivered signal. These functions are not independent material features but are coupled within a single vesicle architecture to establish the spatiotemporal treatment window required to initiate endogenous neurogenesis without introducing cells, genes or implanted stimulation devices. The material platform therefore serves as the primary intervention, with $^1O_2$ acting as the locally generated chemical trigger that links external irradiation to the regenerative response.

In the brain, XSingletO produces a multistage repair outcome rather than a purely neuroprotective or local proliferative effect. The nanovesicles increased NSC proliferation and biased differentiation towards glutamatergic neurons in the traumatic brain injury model. Lineage tracing showed that subventricular-zone-derived newborn cells migrated over millimetre-scale distances along defined anatomical routes to

cortical lesions, repopulated damaged tissue and matured within appropriate laminae. Electrophysiological recordings, retrograde tracing and local-field-potential measurements demonstrated synaptic integration, long-range axonal projection and network-level recovery, accompanied by improvements in motor behaviour. Thus, the treatment generates replacement neurons in situ and recruits them to injury sites, addressing two limitations that commonly constrain transplanted cells: poor lesion-directed migration and incomplete circuit integration.

Compared with existing biomaterial-based strategies for brain repair, XSingletO differs in three design respects. First, most delivery systems achieve either blood–brain barrier crossing or target-cell recognition but not both within a single particle; XSingletO integrates angiopep-2-mediated transcytosis and NFL-TBS-mediated NSC binding in the same vesicle[37–41]. Second, prior X-ray-responsive systems for deep-tissue stimulation have relied on scintillator–photosensitizer pairs that produce diffusible reactive species without spatial confinement[33,48]; here, MMP-2-responsive release and in situ $^1O_2$ generation restrict the redox cue to the NSC microenvironment. Third, previous endogenous-activation approaches have used continuous growth-factor release or genetic manipulation[49-51], whereas XSingletO provides external temporal control and ratiometric dose reporting. These features collectively establish a design principle—integration of sequential targeting, environmentally responsive release, and remote triggering—that may be generalizable to other tissue-regeneration contexts.

Beyond these design advantages, the multi-omics analysis revealed that the neurogenic response initiated by XSingletO was prominently associated with a PPARγ-dependent transcriptional programme, suggesting that the material-generated $^1O_2$ signal may engage this nuclear receptor pathway to orchestrate NSC fate decisions. This finding is independently supported by prior pharmacological studies, in which PPARγ ligands have been shown to regulate NSC proliferation and differentiation, and to improve neuroinflammation and cognitive outcomes in experimental TBI[52,53]. However, the manner in which XSingletO engages this pathway is fundamentally distinct from conventional drug administration. Unlike systemic thiazolidinedione agonists, which

produce sustained peripheral exposure and carry class-associated risks of fluid retention and cardiovascular liability[54], XSingletO delivers a brief, externally timed $^1O_2$ pulse precisely within targeted NSC niches, and its ratiometric reporting capability allows for real-time calibration of the locally delivered signal. Importantly, the multi-omics landscape induced by XSingletO extended well beyond PPARγ activation—encompassing lipid handling, oxidative metabolism, neuronal-state transitions and niche remodelling—indicating that PPARγ serves as a necessary downstream mediator rather than the sole molecular target. This distinction preserves the unique value of the material platform as a spatiotemporally programmable intervention that cannot be recapitulated by direct pharmacological PPARγ activation alone, and reinforces the rationale for pursuing materials-based strategies that integrate targeting, triggering and reporting within a single system.

While these features establish the therapeutic rationale, several issues must be resolved before translation. The therapeutic window for $^1O_2$ generation must be defined across irradiation doses, treatment schedules and lesion volumes, and brain exposure, clearance and off-target oxidative effects should be quantified in large animals. The efficiency of blood–brain barrier transport and NSC-niche targeting may differ with age, chronic inflammation and human neuroanatomy[55-57], particularly because the distance from the human SVZ to many lesions is greater than in mice. The X-ray doses used here (cumulative 126 mGy over three weeks) are substantially below the threshold for deterministic effects in brain tissue[58] and are comparable to the dose from a single head computed tomography scan (approximately 50–100 mGy per scan)[59]. However, the dose-rate dependence of $^1O_2$ generation, the relationship between cumulative dose and neurogenic output, and the potential for cumulative oxidative effects in non-targeted regions require systematic evaluation, particularly in age- and sex-diverse cohorts. The ratiometric reporting capability of XSingletO provides a built-in tool for calibrating $^1O_2$ dose in situ, which may facilitate translation by enabling real-time adjustment of X-ray exposure to achieve the desired redox cue while minimizing off-target effects. Manufacturing consistency, long-term pharmacokinetics, biodegradation and

immunogenicity of the multicomponent vesicle also require systematic evaluation. In addition, although the present experiments were performed in predominantly young adult male mice, studies in females, aged animals and additional acute and chronic brain injuries will be needed to establish the generality of the response.

In summary, XSingletO integrates systemic delivery, blood–brain barrier crossing, NSC-niche targeting and X-ray-triggered $^1O_2$ generation within a single therapeutic material system. By activating endogenous NSCs in situ and directing their neuronal progeny to injured tissue, the platform replaces ex vivo cell expansion and intracranial transplantation with an internally generated repair process. Integrated multi-omics prioritizes a PPARγ-associated programme, and localized *Pparg* loss of function establishes its requirement for the early neurogenic response. This materials-enabled strategy therefore provides a framework for transplantation-free structural and functional regeneration of the injured brain.

References

1. Barker, R. A., Götz, M. & Parmar, M. New approaches for brain repair—from rescue to reprogramming. *Nature* **557**, 329–334 (2018).

2. Nih, L. R., Gojgini, S., Carmichael, S. T. & Segura, T. Dual-function injectable angiogenic biomaterial for the repair of brain tissue following stroke. *Nat. Mater.* **17**, 642–651 (2018).

3. Ghuman, H. et al. Biodegradation of ECM hydrogel promotes endogenous brain tissue restoration in a rat model of stroke. *Acta Biomater.* **80**, 66–84 (2018).

4. Hu, H., Chen, X., Zhao, K., Zheng, W. & Gao, C. Recent advances in biomaterials-based therapies for alleviation and regeneration of traumatic brain injury. *Macromol. Biosci.* **23**, e2200577 (2023).

5. Aertker, B. M., Bedi, S. & Cox, C. S. Jr. Strategies for CNS repair following TBI. *Exp. Neurol.* **275**, 411–426 (2016).

6. Nagahara, A. H. & Tuszynski, M. H. Potential therapeutic uses of BDNF in neurological and psychiatric disorders. *Nat. Rev. Drug Discov.* **10**, 209–219 (2011).

7. Sawamoto, N. et al. Phase I/II trial of iPS-cell-derived dopaminergic cells for Parkinson's disease. *Nature* **641**, 971–977 (2025).

8. Tabar, V. et al. Phase I trial of hES cell-derived dopaminergic neurons for Parkinson's disease. *Nature* **641**, 978–983 (2025).

9. Vieira, R. et al. Young glial progenitor cells competitively replace aged and diseased human glia in the adult chimeric mouse brain. *Nat. Biotechnol.* **42**, 719–730 (2024).

10. Genchi, A. et al. Neural stem cell transplantation in patients with progressive multiple sclerosis: an open-label, phase 1 study. *Nat. Med.* **29**, 75–85 (2023).

11. Trounson, A. & McDonald, C. Stem cell therapies in clinical trials: progress and challenges. *Cell Stem Cell* **17**, 11–22 (2015).

12. Falkner, S. et al. Transplanted embryonic neurons integrate into adult neocortical circuits. *Nature* **539**, 248–253 (2016).

13. Wang, W. et al. Ultrasound-activated piezoelectric nanostickers for neural stem cell therapy of traumatic brain injury. *Nat. Mater.* **24**, 1137–1150 (2025).

14. Zhu, B., Eom, J. & Hunt, R. F. Transplanted interneurons improve memory precision after traumatic brain injury. *Nat. Commun.* **10**, 5156 (2019).

15. Chen, Y.-C. et al. A NeuroD1 AAV-based gene therapy for functional brain repair after ischemic injury through in vivo astrocyte-to-neuron conversion. *Mol. Ther.* **28**, 217–234 (2020).

16. Le, N. et al. Robust reprogramming of glia into neurons by inhibition of Notch signaling and nuclear factor I factors in adult mammalian retina. *Sci. Adv.* **10**, eadn2091 (2024).

17. Wang, M. et al. Nongenetic optical modulation of neural stem cell proliferation and neuronal/glial differentiation. *Biomaterials* **225**, 119539 (2019).

18. Song, M. et al. Optogenetic stimulation of glutamatergic neuronal activity in the striatum enhances neurogenesis in the subventricular zone of normal and stroke mice. *Neurobiol. Dis.* **98**, 9–24 (2017).

763 19. Owusu-Ansah, E. & Banerjee, U. Reactive oxygen species prime Drosophila
764 haematopoietic progenitors for differentiation. *Nature* **461**, 537–541 (2009).
765 20. Sies, H. & Jones, D. P. Reactive oxygen species as pleiotropic physiological signalling
766 agents. *Nat. Rev. Mol. Cell Biol.* **21**, 363–383 (2020).
767 21. Koren, S. A. et al. All-optical spatiotemporal mapping of ROS dynamics across
768 mitochondrial microdomains in situ. *Nat. Commun.* **14**, 6036 (2023).
769 22. Rharass, T. et al. Ascorbic acid alters cell fate commitment of human neural progenitors in
770 a WNT/β-catenin/ROS signalling-dependent manner. *J. Biomed. Sci.* **24**, 78 (2017).
771 23. Shahin, W. S. et al. Redox-dependent Igfbp2 signalling controls Brca1 DNA damage
772 response to govern neural stem cell fate. *Nat. Commun.* **14**, 444 (2023).
773 24. Iwata, R., Casimir, P. & Vanderhaeghen, P. Mitochondrial dynamics in postmitotic cells
774 regulate neurogenesis. *Science* **369**, 858–862 (2020).
775 25. Khacho, M. et al. Mitochondrial dynamics impacts stem cell identity and fate decisions by
776 regulating a nuclear transcriptional program. *Cell Stem Cell* **19**, 232–247 (2016).
777 26. Rafalski, V. A. & Brunet, A. Energy metabolism in adult neural stem cell fate. *Prog.*
778 *Neurobiol.* **93**, 182–203 (2011).
779 27. Le Belle, J. E. et al. Proliferative neural stem cells have high endogenous ROS levels that
780 regulate self-renewal and neurogenesis in a PI3K/Akt-dependant manner. *Cell Stem Cell*
781 **8**, 59–71 (2011).
782 28. Lépinoux-Chambaud, C., Barreau, K. & Eyer, J. The neurofilament-derived peptide NFL-
783 TBS.40-63 targets neural stem cells and affects their properties. *Stem Cells Transl. Med.*
784 **5**, 901–913 (2016).
785 29. Barreau, K., Montero-Menei, C. & Eyer, J. The neurofilament-derived peptide NFL-
786 TBS.40-63 enters in vitro in human neural stem cells and increases their differentiation.
787 *PLoS ONE* **13**, e0201578 (2018).
788 30. Lim, D. A. & Alvarez-Buylla, A. The adult ventricular–subventricular zone (V-SVZ) and
789 olfactory bulb (OB) neurogenesis. *Cold Spring Harb. Perspect. Biol.* **8**, a018820 (2016).

31. Kempermann, G., Song, H. & Gage, F. H. Neurogenesis in the adult hippocampus. *Cold Spring Harb. Perspect. Biol.* **7**, a018812 (2015).

32. Bond, A. M., Ming, G.-L. & Song, H. Adult mammalian neural stem cells and neurogenesis: five decades later. *Cell Stem Cell* **17**, 385–395 (2015).

33. Wang, X. et al. Organic phosphorescent nanoscintillator for low-dose X-ray-induced photodynamic therapy. *Nat. Commun.* **13**, 5091 (2022).

34. Wang, L. et al. Matrix metalloproteinase 2 and MMP9 secreted by erythropoietin-activated endothelial cells promote neural progenitor cell migration. *J. Neurosci.* **26**, 5996–6003 (2006).

35. Koshy, S. T., Ferrante, T. C., Lewin, S. A. & Mooney, D. J. Injectable, porous, and cell-responsive gelatin cryogels. *Biomaterials* **35**, 2477–2487 (2014).

36. Van Hove, A. H., Beltejar, M.-J. G. & Benoit, D. S. W. Development and in vitro assessment of enzymatically responsive poly(ethylene glycol) hydrogels for the delivery of therapeutic peptides. *Biomaterials* **35**, 9719–9730 (2014).

37. Demeule, M. et al. Involvement of the low-density lipoprotein receptor-related protein in the transcytosis of the brain delivery vector Angiopep-2. *J. Neurochem.* **106**, 1534–1544 (2008).

38. Tian, X. et al. On the shuttling across the blood–brain barrier via tubule formation: mechanism and cargo avidity bias. *Sci. Adv.* **6**, eabc4397 (2020).

39. Moreira, R., Nóbrega, C., de Almeida, L. P. & Mendonça, L. Brain-targeted drug delivery: nanovesicles directed to specific brain cells by brain-targeting ligands. *J. Nanobiotechnol.* **22**, 260 (2024).

40. Pucci, C. et al. Chlorin e6-loaded nanostructured lipid carriers targeted by Angiopep-2: advancing photodynamic therapy in glioblastoma. *Adv. Healthc. Mater.* **14**, e2402823 (2025).

41. Carradori, D., Saulnier, P., Préat, V., des Rieux, A. & Eyer, J. NFL-lipid nanocapsules for brain neural stem cell targeting in vitro and in vivo. *J. Control. Release* **238**, 253–262 (2016).

818 42. Zhao, X. & van Praag, H. Steps towards standardized quantification of adult neurogenesis.
819 *Nat. Commun.* **11**, 4275 (2020).
820 43. Osier, N. & Dixon, C. E. The controlled cortical impact model of experimental brain trauma:
821 overview, research applications, and protocol. *Methods Mol. Biol.* **1462**, 177–192 (2016).
822 44. Young, C. C., Brooks, K. J., Buchan, A. M. & Szele, F. G. Cellular and molecular
823 determinants of stroke-induced changes in subventricular zone cell migration. *Antioxid.*
824 *Redox Signal.* **14**, 1877–1888 (2011).
825 45. Chou, F.-S. & Wang, P.-S. Neuronal precursor migration in ex vivo brain slice culture.
826 *Methods Mol. Biol.* **1749**, 135–143 (2018).
827 46. Hansen, K. B. et al. Structure, function, and pharmacology of glutamate receptor ion
828 channels. *Pharmacol. Rev.* **73**, 298–487 (2021).
829 47. Qiu, X. et al. Reversed graph embedding resolves complex single-cell trajectories. *Nat.*
830 *Methods* **14**, 979–982 (2017).
831 48. Matsubara, T. et al. Remote control of neural function by X-ray-induced scintillation. *Nat.*
832 *Commun.* **12**, 4478 (2021).
833 49. Jarkov, V., Califano, D., Tsikriteas, Z. M., Bowen, C. R., Adams, C., & Khanbareh, H. 3D
834 piezoelectric cellulose composites as advanced multifunctional implants for neural stem
835 cell transplantation. *Cell Reports Physical Science* **6**, 102368 (2025).
836 50. Zamproni, L. N., Mundim, M. V., Porcionatto, M. A. & des Rieux, A. Injection of SDF-1-
837 loaded nanoparticles following traumatic brain injury stimulates neural stem cell
838 recruitment. *Int. J. Pharm.* **519**, 323–331 (2017).
839 51. Chai, Y. et al. Structural alignment guides oriented migration and differentiation of
840 endogenous neural stem cells for neurogenesis in brain injury treatment. *Biomaterials* **280**,
841 121310 (2022).
842 52. Morales-Garcia, J. A. et al. Peroxisome proliferator-activated receptor γ ligands regulate
843 neural stem cell proliferation and differentiation in vitro and in vivo. *Glia* **59**, 293–307
844 (2011).

53. Pearson, A. et al. PPARγ activation ameliorates cognitive impairment and chronic microglial activation in the aftermath of r-mTBI. *J. Neuroinflammation* **21**, 194 (2024).

54. Ahmadian, M. et al. PPARγ signaling and metabolism: the good, the bad and the future. *Nat. Med.* **19**, 557–566 (2013).

55. Baig, S. et al. Identity and nature of neural stem cells in the adult human subventricular zone. *iScience* **27**, 109342 (2024).

56. Kalamakis, G. et al. Quiescence modulates stem cell maintenance and regenerative capacity in the aging brain. *Cell* **176**, 1407–1419.e14 (2019).

57. Tracy, G. C. et al. Intracerebral nanoparticle transport facilitated by Alzheimer pathology and age. *Nano Lett.* **23**, 10971–10982 (2023).

58. ICRP. ICRP statement on tissue reactions and early and late effects of radiation in normal tissues and organs—threshold doses for tissue reactions in a radiation protection context. ICRP Publication 118. *Ann. ICRP* **41**, 1–322 (2012).

59. McCollough, C. et al. Diagnostic reference levels from the ACR CT Accreditation Program. *J. Am. Coll. Radiol.* **8**, 795–803 (2011).

Methods

Mouse models

All animal procedures conformed to the Guide for the Care and Use of Laboratory Animals and were approved by the Animal Protection and Use Committee of East China Normal University (approval number m+R20190304, Shanghai, China). Male C57BL/6J, Rosa26-LSL-EGFP reporter mice *Pparg* $^{fl/fl}$ *mouse* (4–6 weeks of age; Shulaibao (Wuhan) Biotechnology Co., Ltd.) were maintained under specific pathogen–free (SPF) conditions on a 12 h light/12 h dark cycle (22 ± 2°C; 55 ± 10% humidity) with ad libitum access to food and water.

Animals were weighed three times per week; mice showing >15% body weight loss, hunched posture, or persistent neurological deficits were humanely euthanized according to institutional guidelines. Mice were block-randomized by body mass and

litter, and all behavioral, histological, and electrophysiological assessments were performed by investigators blinded to group allocation. The number of animals used in each experiment and per treatment group is reported in the corresponding figure legends. Only male mice were used in this study, and no sex-based analyses were performed.

Traumatic brain injury model

Traumatic brain injury (TBI) was induced using a controlled cortical impact (CCI) model in C57BL/6J or Rosa26-LSL-EGFP mice. Under isoflurane anesthesia, a 4 × 4 mm craniotomy was made over the right primary motor cortex (M1; centered at coordinates matching the right M1 region), taking care not to damage the dura. A 3.0 mm flat-tip impactor was driven at 4.5 m s^{-1} to a depth of 1.8 mm with a dwell time of 300 ms. The bone flap was replaced and sealed with bone wax, the scalp was sutured, and mice were allowed to recover on a heated pad. Sham-operated controls underwent identical anesthesia and craniotomy but no impact.

For lineage-tracing experiments, AAV-SCH9-Sox2-Cre was stereotaxically injected into either the subventricular zone (SVZ) or subgranular zone (SGZ) of Rosa26-LSL-EGFP mice one week before CCI, thereby labeling NSCs and their progeny with EGFP. Following TBI, mice were assigned to vehicle/sham, irradiation-only, XSingletO-only, or XSingletO + X-ray activation cohorts as detailed in the Method Details and figure legends.

Preparation of XSingletO nanovesicles

The three-step fabrication—including gelatin methacrylation, GPLGVC grafting, ITC/RatioCL co-encapsulation and dual-peptide surface decoration—is described in detail in **Extended Data Fig. 1a**. Gelatin was first methacrylated by reacting with methacrylic anhydride under stirring, followed by dialysis and lyophilization to yield methacrylated gelatin (MA-Gel). The MMP-2–cleavable peptide GPLGVC was conjugated to MA-Gel through carbodiimide chemistry to obtain MA-Gel-GPLGVC. This precursor was emulsified in chloroform containing 2% Span-80 at an aqueous-to-oil ratio of approximately 1:10 and subsequently photopolymerized under UV

irradiation (365 nm, 10 mW cm^{-2}, 5 min). The resulting hydrogel cores were stabilized by brief cross-linking with 0.1% glutaraldehyde and quenched with glycine.

The vesicles were further modified with NHS-PEG_{3400}-maleimide, enabling thiol–maleimide conjugation of the BBB-penetrating peptide angiopep-2 and the NSC-tropic peptide NFL-TBS. For therapeutic loading, the organic phosphorescent scintillator ITC and ratiometric chemiluminescent probe RatioCL[33,60,61] were co-encapsulated by introducing them into the aqueous phase before emulsification. After centrifugation and repeated PBS washing to remove unreacted reagents, the vesicles were characterized by dynamic light scattering for size distribution and transmission electron microscopy for morphology. Endotoxin content was confirmed to be <0.25 EU mg^{-1} using a Limulus Amebocyte Lysate assay. For in vivo tracking, Cy7 or Alexa Fluor 488 labels were incorporated into the vesicle shell by premixing corresponding fluorescent dyes into the organic phase.

Physicochemical characterisation.

The hydrodynamic diameter of XSingletO vesicles was 80.2 ± 4.7 nm with a polydispersity index (PDI) of 0.12, as determined by dynamic light scattering. The ζ-potential was -18 ± 2 mV under neutral pH conditions, indicative of moderate colloidal stability. Transmission electron microscopy confirmed a uniform spherical morphology (**Fig. 1b**). Fourier-transform infrared spectra showed characteristic amide and methacrylate peaks as well as new bands corresponding to peptide and fluorophore conjugation. Vesicles remained colloidally stable for at least 14 days in PBS or 10 % FBS at 37°C without aggregation, as verified by DLS size monitoring (**Extended Data Fig. 2a-c**).

X-ray dosimetry and $^1O_2$ quantification

Dosimetry was performed using an Unfors Xi detector positioned at brain-surface depth beneath a 15 mm lead collimator. Unless otherwise stated, animals or samples were irradiated at 30 μGy s^{-1} (150 kVp, 1 mA, source-to-sample distance 30 cm, added filtration 2.0 mm Al) for 10 min (cumulative dose = 18 mGy). Beam homogeneity was

verified by laterally scanning the detector in 2 mm steps across the 15 mm field, with uniformity within ± 5%.

In vitro $^1O_2$ production was quantified with Singlet Oxygen Sensor Green (SOSG, Thermo; ex 504 nm/em 525 nm) following the manufacturer's instructions, measuring n = 3 replicates per condition on a SpectraMax iD5 plate reader (200 µL per well, read from the bottom, integration time 0.5 s, temperature 22-25ºC). In situ $^1O_2$ was monitored ratiometrically using the RatioCL probe as F_{720}/F_{773}; readings were acquired within 2 min post-irradiation to minimize secondary reactions.

Trans-BBB transport assay

A tri-culture Transwell model (0.4 µm pore size, Corning) was established to reconstitute the blood–brain barrier (BBB) in vitro, using primary murine brain microvascular endothelial cells, rat astrocytes, and pericytes, adapted from established primary-cell tri-culture BBB models[62]. Astrocytes and pericytes were seeded on the abluminal side of collagen IV/fibronectin-coated inserts 24 h prior to endothelial cell seeding on the luminal surface. Cells were seeded at a ratio of 4:2:1 (endothelial: astrocyte: pericyte, 1.2×10^5: 6.0×10^4: 3.0×10^4 cells cm^{-2} and maintained for 5-7 days until confluence was achieved. Monolayer integrity was confirmed by TEER values ≥200 $\Omega \cdot cm^2$ measured with an EVOM^2 voltohmmeter (World Precision Instruments). Cy7-labelled XSingletO vesicles (200 µg mL^{-1} in serum-free DMEM, applied to the apical chamber in 500 µL volume) were incubated at 37ºC, 5% CO_2. Basolateral samples (200 µL) were collected at 0-6 h, replaced with fresh medium to maintain sink conditions, and fluorescence was measured (λ_{ex} 750 nm, λ_{em} 777 nm) on a SpectraMax iD5 plate reader (Molecular Devices) using auto-gain mode, 0.5 s integration time, 9 nm bandwidth.

The apparent permeability coefficient (P_app) was calculated according to Fick's law:

$$P_app = (dQ/dt) / (A \times C_0)$$

where dQ/dt is the steady-state flux across the monolayer, A is the membrane surface area (1.12 cm^2 for 12-well inserts), and C_0 is the initial apical concentration. All assays were performed in triplicate independent inserts (n = 3).

Primary NSC culture and in-vitro assays

Neural stem cells (NSCs) were isolated from the subventricular zone (SVZ) of adult C57BL/6 mice by papain dissociation (20 U mL^{-1}, 30 min at 37ºC, DNase I 0.005% w/v) followed by Sox2-based magnetic sorting (Miltenyi Biotec). Cells were seeded at 5×10^4 cm^{-2} on poly-D-lysine/laminin-coated coverslips (13 mm, Corning) and cultured in Neurobasal-A medium supplemented with B27 (2%), GlutaMAX (2 mM), penicillin/streptomycin (1%), EGF (20 ng mL^{-1}) and FGF-2 (20 ng mL^{-1}). Cy7-labelled or unlabelled XSingletO vesicles (10 µg mL^{-1}) were added for 4 h, washed three times with PBS, and irradiated under X-ray conditions described above. Cell proliferation was assessed 48 h later using EdU incorporation (Click-iT EdU Alexa Fluor 594 kit, Thermo Fisher, 10 µM EdU, 2 h pulse). Differentiation was evaluated 7 d post-irradiation by immunocytochemistry for βIII-tubulin (neurons; 1:500, Abcam) and GFAP (astrocytes; 1:500, Dako), followed by Alexa Fluor secondary antibodies (1:1000, Invitrogen). Nuclei were counterstained with DAPI (1 µg mL^{-1}), and samples were imaged with a Leica TCS SP8 confocal microscope (20×/0.75 NA, laser ex 488/561 nm, pinhole 1 AU, z-step 1 µm). Quantitative morphometry of neurite length and branching number was performed on at least 30 cells per condition (n = 3 independent cultures) using Neurolucida 360 (MBF Bioscience).

Systemic administration and pharmacokinetics

C57BL/6 mice received tail-vein injections of XSingletO nanovesicles (5 mg kg^{-1}, in 100 µL sterile PBS). Whole-body near-infrared fluorescence imaging was performed with an IVIS Spectrum system (PerkinElmer; λex/λem = 710/780 nm, exposure time 1–3 s, binning medium, f-stop 2) at 0.5, 2, 6, 12, 24 and 48 h, and 7 d post-injection. Regions of interest (brain, liver, spleen, kidney, lung) were manually delineated, and fluorescence intensity was quantified using Living Image software v4.7. For ex vivo

biodistribution, mice were euthanized at 12 h and 48 h (n = 3 per time point), organs were excised, washed in PBS, and imaged under the same settings. Signal values were normalized to injected dose per gram of tissue (ID % g^{-1}) and corrected for background autofluorescence measured from uninjected controls.

Viral vectors and stereotaxic injections

For lineage tracing, AAV-SCH9-Sox2-Cre (3×10^{12} vg mL^{-1}, BrainVTA, diluted 1:1 in PBS before injection) was delivered into either the subventricular zone (SVZ; AP +0.5, ML +1.0, DV –2.2 mm) or the subgranular zone (SGZ; AP –2.0, ML +1.6, DV –2.0 mm) of Rosa26-LSL-EGFP reporter mice by stereotaxic injection. Injections were performed under 2% isoflurane anesthesia, using a 33-gauge Hamilton micro syringe at 0.1 μL min^{-1}, with a total volume of 1 μL per site. The needle was left in place for 5 min post-injection to minimize backflow before slow withdrawal. Viral delivery occurred one week before injury.

For optogenetic experiments, AAV2-SCH8-CMV-hChR2(H134R)-mCherry (2×10^{12} vg mL^{-1}, 1 μL) was injected peri-lesion (AP 0, ML +1.0, DV –1.0 mm) under identical conditions. At 15 weeks post-TBI, acute coronal brain slices were prepared from the peri-lesional cortex, and whole-cell patch-clamp recordings were performed from $EGFP^+$ newborn neurons while ChR2-$mCherry^+$ host neurons were optically stimulated.

Controlled cortical-impact traumatic brain injury

Traumatic brain injury was induced in C57BL/6 mice and Rosa26-LSL-EGFP reporter mice using a home-made controlled cortical impactor (CCI). Animals were anesthetized with isoflurane (3% for induction and 2% for maintenance) delivered in a carrier gas mixture of 70% N_2 and 30% O_2 and secured in a stereotaxic frame with a heating pad to maintain body temperature at 37ºC. After midline scalp incision and periosteal removal, a 4 × 4 mm craniotomy was performed over the right primary motor cortex (M1), using coordinates matching the Results section, taking care not to damage the dura. A 3.0 mm flat-tip impactor was driven at 4.5 m s^{-1} to a depth of 1.8 mm with a dwell time of 300 ms. After impact, the bone flap was replaced and sealed with bone

wax, the scalp was sutured, and mice were allowed to recover on a heated pad. Analgesia was provided with buprenorphine (0.1 mg kg^{-1}, s.c.) immediately post-surgery and every 12 h for 48 h. Control mice underwent identical anesthesia and craniotomy but without impact. One week before CCI, AAV-SCH9-Sox2-Cre was stereotactically injected into the SVZ or SGZ of Rosa26-LSL-EGFP mice to label NSCs and their progeny. Migrating newborn neurons entering the peri-lesional cortex were intrinsically $EGFP^+$, enabling longitudinal tracking.

Therapeutic regimen

Mice received intravenous (i.v.) administration of XSingletO nanovesicles (5 mg kg^{-1} in 100 μL sterile PBS, tail vein). The formulation comprises an MMP-2–responsive gelatin shell and BBB-penetrating ANG peptides to enhance brain delivery. To trigger on-demand $^1O_2$ generation in the brain, X-ray activation was applied 12 h post-injection at 30 μGy s^{-1} for 10 min (≈ 18 mGy per session) under identical exposure parameters across groups. Unless stated otherwise, a condensed schedule was used in all experiments: activation every 3 days for 3 weeks (7 sessions; ≈ 126 mGy cumulative). Animals were randomized to treatment, and experimenters were blinded during imaging, quantification, and endpoint analyses. Control arms included XSingletO-only, irradiation-only, and sham groups, as appropriate. Health monitoring (body weight, activity) was recorded throughout the study.

Immunofluorescence and histology

Mice were deeply anesthetized and transcardially perfused with ice-cold PBS followed by 4% paraformaldehyde (PFA). Brains were post-fixed in 4% PFA for 12–16 h at 4ºC, cryoprotected in 30% sucrose until sinking, and embedded in OCT. Coronal sections (20 μm) were cut on a cryostat (Leica CM1950) and stored in cryoprotectant at -20ºC until use. Free-floating sections were blocked/permeabilized in 5% normal donkey serum + 0.3% Triton X-100 in PBS for 1 h (RT), then incubated overnight at 4ºC with primary antibodies (see panel below). After 3 × 10 min PBS washes, sections were incubated with donkey secondary antibodies (Invitrogen; Alexa Fluor 488/555/647;

1:1000, 2 h, RT), washed, and counterstained with DAPI (1 μg mL^{-1}, 10 min). Sections were mounted in antifade medium and imaged under identical acquisition settings across groups. BrdU note: Before BrdU immunostaining, DNA was denatured in 2 N HCl (30 min, RT), neutralized with 0.1 M borate buffer (pH 8.5, 10 min), then processed as above. Primary antibodies: DCX (rabbit; Abcam, e.g., 1:500); Sox2 (rabbit; Cell Signaling Technology, 1:500); MAP2 (chicken; Abcam, 1:1000); BrdU (guinea pig; Abcam, 1:200; with HCl denaturation); GFAP (rabbit; Abcam, 1:1000); anti-EGFP/GFP (chicken; Aves Labs, 1:1000); Olig2 (rabbit; Abcam, 1:500); Cux1 (rabbit; Oasis, 1:500); Ctip2 (Bcl11b) (guinea pig, Oasis,1:500); NeuN (mouse; MilliporeSigma MAB377-class, 1:1000). Secondary antibodies: Donkey anti-rabbit/mouse/guinea pig/chicken Alexa Fluor 488/555/594/647 (Yeasen), 1:1000, 2 h at RT, protected from light.

Images were acquired on a Zeiss LSM 880 confocal microscope equipped with Airyscan (Plan-Apochromat 40×/1.3 NA oil or 63×/1.4 NA oil objectives, pinhole 1 AU, z-step 0.3-0.5 μm, laser power adjusted to avoid saturation) and processed using Imaris 9.9 (Bitplane). Cell counts were averaged over three anatomically matched sections per mouse (n = 3-5 mice per group). Dendritic spine density was quantified from MAP2-positive dendritic segments (≥ 50 μm length) in lineage-traced newborn neurons, and spines were classified according to standard morphological criteria.

Flow cytometry

The SVZ and SGZ tissues were rapidly dissected from adult C57BL/6 mice and enzymatically dissociated using the Adult Brain Dissociation Kit (Miltenyi Biotec) according to the manufacturer's instructions. The resulting single-cell suspensions were passed through a 40-μm cell strainer and washed in ice-cold PBS supplemented with 2% FBS. Cells were then fixed and permeabilized using a fixation/permeabilization buffer according to the manufacturer's instructions before intracellular or nuclear marker staining. For cell typing, cells were incubated with Fixable Viability Dye 780 (eBioscience, 1:1000, 15 min at 4°C in the dark) to exclude dead cells, followed by staining with fluorophore-conjugated antibodies, MAP2-AF647, and GFAP-

BV421(BioLegend, typical dilution 1:200). After staining, cells were washed twice in PBS/2% FBS and resuspended at 1×10^6 cells mL^{-1} for acquisition. For analysis of cell apoptosis, cells were stained with Annexin V–FITC/PI in Ca^{2+}-containing binding buffer (1×, 15 min, RT, dark), and acquired immediately. Gating proceeded as FSC/SSC-singlets-live cells (PI^-), then Annexin V^+/PI^- (early apoptosis) and Annexin V^+/PI^+ (late apoptosis/necrosis) were quantified. Unstained, single-stained, and compensation controls were included; staurosporine-treated cells served as a positive control.

Flow cytometry was performed on a BD LSRFortessa cytometer (equipped with 405, 488, 561 and 640 nm lasers, PMT voltages adjusted for each fluorophore). At least 10,000 live events per sample were recorded. Single-stain controls were prepared with UltraComp eBeads (Thermo Fisher) for compensation, and fluorescence minus one (FMO) controls were used to define gating thresholds. Data were analysed with FlowJo v10 using standard sequential gating (FSC/SSC, singlets, live cells, marker expression).

Electrophysiology

Acute coronal brain slices (300 μm) were prepared from mice at 15 weeks post-TBI using a vibratome (Leica VT1200S) in ice-cold cutting solution (in mM: 75 sucrose, 80 NaCl, 2.5 KCl, 1.25 NaH_2PO_4, 25 $NaHCO_3$, 25 glucose, 7 $MgCl_2$, 0.5 $CaCl_2$, oxygenated with 95% O_2/5% CO_2). Slices were recovered for 30 min at 34ºC in ACSF and then maintained at room temperature until recording. Whole-cell patch-clamp recordings were obtained from EGFP-labelled newborn neurons located in the peri-lesional cortex, perfused with oxygenated ACSF at 32ºC (in mM: 125 NaCl, 2.5 KCl, 1.3 $MgCl_2$, 2.5 $CaCl_2$, 1.25 NaH_2PO_4, 26 $NaHCO_3$, 20 glucose). Patch pipettes (3-5 MΩ) were filled with an internal solution containing (in mM): 135 K-gluconate, 10 HEPES, 2 $MgCl_2$, 0.25 EGTA, 4 Mg-ATP, 0.3 Na-GTP, and 10 phosphocreatine (pH 7.3, 290 mOsm). Series resistance was monitored throughout, and cells with Rs >20 MΩ or >20% change were excluded. ChR2-expressing host neurons were optically stimulated with a 470 nm LED (2 mW mm^{-2}, 5-15 ms pulses) delivered via the epifluorescence pathway. Light-evoked excitatory postsynaptic potentials (EPSPs)

were recorded from $EGFP^+$ newborn neurons in current-clamp mode. Pharmacological blockade with NBQX (10 μM) and CPP (20 μM) confirmed AMPA and NMDA receptor mediation. Signals were amplified with a MultiClamp 700B amplifier (Molecular Devices), digitised at 10 kHz, and acquired through a CED Power1401 interface using Spike2 software (Cambridge Electronic Design, UK), with data stored in native. For statistical analysis, electrophysiological measurements were reported as both recorded-cell number and mouse number; no more than three cells were analyzed from the same animal for a given comparison, and animal-level means were used for confirmatory group statistics.

Local-field-potential (LFP) recording

Tripolar tungsten electrodes (Ø 50 μm, impedance ~300 kΩ at 1 kHz; FHC) were stereotaxically implanted into the peri-lesional cortex (AP 0 mm, ML +1.5 mm, DV -1.0 mm relative to bregma) and secured with anchor screws and acrylic dental cement. A reference electrode was placed in the cerebellar hemisphere. Animals recovered for ≥ 7 d before recording.

Signals were acquired with a Plexon OmniPlex system in pl2 format, band-pass filtered at 1–1,000 Hz, and digitised at 10 kHz. Data were analysed in NeuroExplorer 5.0 (Nex Technologies), where power spectral density was computed using Welch's method (256-sample Hamming window, 50% overlap) and multiscale sample entropy was calculated with embedding dimension m = 2 and tolerance r = 0.15 × SD over scales 1–20. Processed datasets were exported and visualized in OriginPro 2023 (OriginLab).

Behavioural assays

All behavioral tests were conducted during the light cycle in a dedicated behavioural suite maintained at 21°C with controlled noise and illumination. Mice were acclimated to the testing room for 30 min prior to each trial, and apparatuses were cleaned with 70% ethanol between animals. Motor coordination was assessed with an accelerating rotarod (Ugo Basile) from 4 to 40 r.p.m. over 5 min; the latency to fall was recorded and averaged over three trials per day (inter-trial interval ≥15 min). Voluntary wheel running

was monitored with a low-profile wireless wheel system, and cumulative distance travelled was logged during the 12-h dark phase. Working memory was evaluated using a T-maze spontaneous alternation task (15 trials per session). An alternation rate ≥70% was defined as intact working memory. All behavioural analyses were performed by investigators blinded to experimental groups.

Single-nucleus RNA sequencing

1. Preparation of single-nucleus suspensions

After the removal of adipose tissue and necrotic tissue from the tissue samples, the samples were rinsed with pre-cooled DPBS at 4ºC for 2-3 times. For brain tissues, samples were instead incubated in a papain-based dissociation solution (e.g., Papain Dissociation System, Worthington Biochemical) supplemented with DNase I (0.1 mg/mL) and gently triturated in Hibernate-A medium (Gibco) on ice to obtain a single-nucleus suspension, avoiding mechanical dissociation by gentleMACS. Next, all single-nucleus suspensions were filtered through 70 μm or 40 μm cell strainers and centrifuged at 4ºC. After removing the supernatant, the cell pellet was resuspended in 1 mL of cell resuspension solution. 3 mL red blood cell lysis buffer was added, and the sample was incubated on ice for 2-10 min. To stop lysis, 6 mL DMEM containing 5% weight/volume FBS was added. At last, the supernatant was discarded after centrifugation at 4ºC and the pellet was resuspended in 1mL above mixture for the first subsequent cell quality inspection.

2. Inspection of single-cell suspension

After treating with AO/PI double fluorescent dye, cell quality was conducted on Countstar Rigel S2 to determine cell concentration, cell viability and cell clump.

3. Single-nucleus RNA-seq library preparation

After quality inspection, cell concentration of the single-nucleus suspensions was adjusted to 216 cells/μL, and then single nucleus capture and library construction were performed according to the instructions of the DECODER single nucleus 3‘kit v1.0 (Dynamic Biosystems, 13010023).

4. Single-nucleus RNA-seq library sequencing

The final library pool was sequenced on the Illumina NovaSeq 6000(MGI T7) instrument using 150-bp paired-end reads.

5. snRNA-seq data processing and quality control

Raw sequencing reads were aligned to the mouse reference genome (mm10) using Cell Ranger (version 7.0.1, 10x Genomics) with default parameters to generate the gene-barcode matrices. Subsequently, the Seurat R package (version 4.3.0)[63] was employed to conduct single- nucleus analyses. Initial quality control was performed by assessing feature counts and mitochondrial counts. Cells were flagged for exclusion if their feature or mitochondrial counts exceeded the 99th percentile threshold. Additionally, cells with feature counts or unique molecular identifier (UMI) counts below 200 and 500, respectively, were filtered out to ensure sufficient sequencing depth. Genes detected in fewer than three cells were also excluded to maintain data reliability. Doublet detection was facilitated by the doubletFinder tool (version 2.0.3),[64] which helped identify and remove potential doublets from the dataset. Data normalization was carried out using Seurat's LogNormalize function to prepare the gene counts matrix for downstream analysis. The Seurat workflow was then followed for scaling and principal component analysis (PCA). To further explore the data, we employed the Uniform Manifold Approximation and Projection (UMAP)[65] for visualization. To mitigate batch effects across samples, Harmony (version 0.1.1)[66] was integrated into our analysis pipeline. Cells were clustered using the Louvain method, and UMAP was utilized to visualize the clusters based on principal components that cumulatively contributed to a variance of greater than 85%. The FindAllMarkers function was subsequently applied to identify differentially expressed marker genes for each cluster, using the default Wilcoxon rank sum test method.

6. Cell type identification

Cell types were identified by marker genes selected from previous studies and CellMarker database[67]. The main cell types were defined based on cell-type-restricted

enrichment of specific markers: neuronal clusters selectively expressed *Rbfox3, Snap25, Syt1, Satb1, Satb2,* and *Syn1*; astrocytes expressed *Aqp4, Aldh1l1, Slc1a3,* and *Gfap*; microglial cells were enriched for *Aif1, P2ry12, Cx3cr1,* and *C1qa*; OPCs expressed *Pdgfra, Cspg4,* and *Vcan*; and oligodendrocytes expressed myelin-associated genes such as *Mbp, Plp1,* and *Mog.*

7. ORA enrichment analysis

Over-representation analysis (ORA) was performed to identify biological processes and signaling pathways associated with differentially expressed genes (DEGs) derived from snRNA-seq, spatial transcriptomics, and proteomic datasets. DEGs were determined using a Wilcoxon rank-sum test with Benjamini–Hochberg correction (adjusted $p < 0.05$ and $|\log_2 FC| > 0.25$). Enrichment analyses were conducted using the clusterProfiler R package (v4.6.0)[68]. Both Gene Ontology (GO)—covering biological process (BP), molecular function (MF), and cellular component (CC) categories—and Kyoto Encyclopedia of Genes and Genomes (KEGG) pathway analyses were performed.

For GO enrichment, genes were annotated against the org.Mm.eg.db database (v3.17.0), and pathways with $p < 0.05$ and $q < 0.05$ were considered significant. KEGG enrichment used the KEGG.db (v3.17.0) annotation, with results ranked by gene ratio and enrichment score. Visualization was performed using enrichplot and ggplot2, generating dot plots and bar plots highlighting the top 20 enriched terms for each dataset.

Spatial transcriptomics

1. Preparation of spatially barcoded arrays

The DynaSpatial FFPE Spatial Gene Expression Slides & Reagents Kits for Mouse Transcriptome were obtained from Dynamic Biosystems (Suzhou, China). The gene expression slides were used to generate spatially barcoded cDNA from tissue sections following the manufacturer's instructions. Each barcoded DNA array on the slide contained 5,265 spots with unique barcoded oligonucleotides and poly(dT)VN within a 7.5 x 7.5 mm^2 capture area. Each spot measured 50 μm in diameter, with a center-to-

center distance of 100 μm between adjacent spots. A fiducial frame was printed as a border around the capture areas to ensure proper orientation.

2. Preparation of tissue slides

For FFPE tissue sections, paraffin-embedded brain tissues were sectioned at 5–10 μm and mounted on DynaSpatial slides according to the manufacturer's FFPE protocol.

3. H&E staining and imaging

Tissue sections were stained with H&E and imaged using the Pannoramic MIDI II automatic digital slide scanner (3DHISTECH, Hungary) under brightfield conditions to obtain structural information about the tissue.

4. Probe hybridization, ligation, release and capture

For FFPE tissues, a probe mix targeting a large gene panel was directly added to the tissue sections for hybridization, followed by probe ligation[69]. The ligated probes were then released from the tissue slides and captured by poly(dT)VN on the Spatial Gene Expression Slides using the Dynablot system (Dynamic Biosystems, Suzhou, China). Subsequently, the captured probes were extended.

5. Library construction and sequencing

The extended probe products were denatured and transferred from the capture area to a new tube, where they were amplified via Polymerase Chain Reaction (PCR) to generate sufficient material.

The sequencing library was then prepared following the DynaSpatial library preparation protocol (Dynamic Biosystems, Suzhou, China). Quality inspection of the final library was performed using the Qubit 4.0 fluorometer and dsDNA HS Assay Kit (Thermo, Q32854) to measure concentration and the Agilent 4150 High Sensitivity D5000 TapeStation to assess library integrity. Finally, paired-end 150 bp sequencing (150PE mode) was conducted on the Illumina NovaSeq X Plus platform.

6. Spatial transcriptomic data processing and quality control

Raw sequencing reads were aligned to the mouse reference genome (mm10) using DynamicST (version 1.0.1, Dynamic Biosystems, Suzhou, China) according to the DynaSpatial manufacturer's protocol. Subsequently, the Seurat R package (version 4.3.0)[63] was employed to conduct spatial transcriptomic analyses. Technical variability within data was reduced with SCTransform[70] (SCTransform() with default settings; SelectIntegrationFeatures() with nfeatures = 3000; PrepSCTIntegration() with anchor.features assigned to genes returned from the SelectIntegrationFeatures()) and Harmony[66] (RunHarmony() with group.vars = 'section.name' addressing for batches associated with different tissue sections/samples) packages. Principal Component Analysis (PCA) was used for selection of significant components. FindClusters() with resolution = 0.6 was used to identify clusters and then Uniform Manifold Approximation and Projection (UMAP)[65] was used to visualize the same in 2D space.

7. Spatial mapping of *Dcx*$^+$ newborn neurons and developmental gene sets

Spatial transcriptomic data were processed using stLearn (v0.4.0)[71] and Seurat (v4.3.0). Spots expressing neuronal lineage marker *Dcx* were defined as immature neurons, and their spatial coordinates were extracted from tissue sections encompassing the SVZ and perilesional cortex. Expression scores for NSC-related gene set (*Nes*, *Sox2*, *Msi1*, *Prom1*, and *Pax6*) were calculated using the AddModuleScore function in Seurat and normalized to total UMI counts per spot. The resulting module scores were projected onto the tissue coordinates using stLearn.spatial_plot, generating heatmaps of gene-set activity across regions and time points. To infer migratory trajectories, spatial gradient analysis was performed by quantifying radial intensity changes of *Dcx*+ signals and NSC-related gene set module scores from the SVZ toward the cortical lesion border. The gradual decrease in NSC-related gene set and concomitant increase in *Dcx* signal intensity delineated a directional migration axis of newborn neurons during repair. For **Extended Data Fig. 6**, *Dcx*-enriched regions and NSC-related-gene-set-high domains were defined using the section-wise upper quartile of normalized *Dcx* expression or AddModuleScore values, followed by spatial-contiguity filtering to exclude isolated single-spot signals. Threshold sensitivity was evaluated by repeating the analysis at the

70th and 80th percentiles and confirming preservation of the SVZ-to-lesion spatial trend.

PPAR-family prioritization was performed across the neuronal populations used for the neurogenesis-related module-score analysis. For snRNA-seq, Seurat DotPlot was used to summarize the percentage of nuclei with detectable expression and the scaled average expression of *Ppara*, *Ppard*, *Pparg* and selected PPAR-associated lipid-metabolic genes across Control, TBI, Week 3, Week 9 and Week 15. For spatial transcriptomics, neuron-annotated spots were subset from each section, and *Ppara*, *Ppard* and *Pparg* expression was projected onto tissue coordinates. The percentage of positive neuronal spots and mean normalized expression were summarized for TBI, Week 9 and Week 15. These analyses were used to assess cross-platform consistency among PPAR-family members rather than to infer receptor activity from transcript abundance alone.

Proteomics

The SVZ tissue (10 mg per sample) was homogenized in ice-cold RIPA buffer (Thermo Fisher 89900) supplemented with protease and phosphatase inhibitors (Roche 11836170001) using a bead-mill homogeniser (Qiagen TissueLyser II) at 30 Hz for 2 min × 3 cycles. Lysates were cleared by centrifugation at 14,000 g for 10 min at 4°C, and protein concentration was determined by BCA Protein Assay Kit (Thermo Fisher 23225). Equal aliquots (100 μg per sample) were digested with sequencing-grade trypsin/Lys-C (Promega V5071, 1:50 enzyme:substrate ratio, overnight at 37°C) and labelled with TMT 11-plex reagents[72] (Thermo Fisher 90111) according to the manufacturer's instructions. Peptide mixtures were fractionated and separated on an UltiMate 3000 RSLCnano system (Thermo) and analysed on an Orbitrap Eclipse mass spectrometer equipped with FAIMS interface, using SPS-MS3acquisition (Top10 method, NCE 45%, resolution 120,000 at m/z 200, AGC target 4e5, max injection time 50 ms). Data were processed with MaxQuant[73] v2.2 against the UniProt Mus musculus

reference proteome (release 2023-06), with a 1% FDR at peptide and protein levels. Differentially expressed proteins were defined as fold change ≥1.5, FDR <0.05, and visualized in Perseus[74]. Functional enrichment was assessed using STRING (v11.5)[75].

Western blotting

Key signaling and lineage-associated proteins were validated by Western blotting. Equal amounts of protein (20–30 μg per lane) were resolved on 10% SDS–PAGE gels and transferred to PVDF membranes (0.45 μm, Millipore). Membranes were blocked with 5% BSA in TBST for 1 h at room temperature and incubated overnight at 4ºC with primary antibodies against PPARγ (Cell Signaling Technology, 1:1000), PDK4 (Abcam, 1:1000), FABP7 (Proteintech, 1:1000), CPT1A (Abcam, 1:1000), DCX (Abcam, 1:1000), NeuroD1 (Cell Signaling Technology, 1:1000), Tuj1 (βIII-tubulin; Sigma, 1:2000), and GFAP (Cell Signaling Technology, 1:2000). After washing, membranes were incubated with HRP-conjugated anti-rabbit or anti-mouse secondary antibodies (1:5000, Cell Signaling Technology) for 1 h at room temperature. Protein bands were visualized using enhanced chemiluminescence (ECL; GE Healthcare) on a ChemiDoc MP imaging system (Bio-Rad). Band intensities were quantified in ImageJ and normalized to β-actin (Proteintech, 1:5000) or GAPDH (Abcam, 1:5000).

Statistics and reproducibility

All statistical analyses were performed using GraphPad Prism 10 (GraphPad Software) and R version 4.3. Prior to hypothesis testing, data distributions were examined for normality using the Shapiro-Wilk test. For normally distributed data, comparisons between two groups were made using unpaired two-tailed Student's t-tests, whereas comparisons across multiple groups employed one-way ANOVA followed by Tukey's multiple-comparisons test (two-sided). Repeated-measures data were evaluated using a mixed-effects model with Geisser-Greenhouse correction. For non-normally distributed data, Mann-Whitney U tests (two groups) or Kruskal-Wallis tests with Dunn's multiple-comparison post hoc were applied. For all figure panels, the exact biological sample size, definition of n, statistical test, and multiple-comparison correction are indicated in

the corresponding figure legends whenever applicable. Where technical replicates were present, they were first averaged within each biological replicate before group-level statistical testing.

Electrophysiological input-output relationships were compared using extra-sum-of-squares F-tests. Outliers were identified prospectively using a 1.5 × IQR criterion and excluded only if attributable to technical error. Sample sizes were determined by a priori power analysis (G*Power v3.1[76], $\alpha = 0.05$, $\beta = 0.8$) anticipating an effect size of ~30%. Data are reported as mean ± s.d. unless otherwise specified, with statistical significance set at $p < 0.05$. For omics analyses, adjusted p values or false discovery rate (FDR) values were reported where pathway enrichment or genome-wide testing was performed. All datasets were coded prior to analysis, and investigators remained blinded to group assignments during quantification. Genome-wide and pathway-level multiple testing was controlled using Benjamini-Hochberg FDR correction unless otherwise specified.

Data availability

Raw sequencing data generated in this study have been deposited in the NCBI Sequence Read Archive under BioProject accession numbers PRJNA1475752 for single-nucleus RNA-seq and PRJNA1475873 for spatial transcriptomics. Processed single-nucleus RNA-seq and spatial transcriptomics data have been deposited in GEO under accession numbers GSE334661 and GSE334663, respectively.

All other data supporting the findings of this study are available within the paper and its Supplemental Information or from the lead contact upon reasonable request.

Code availability

This paper does not report original code. All analyses were performed using publicly available software and packages listed in the key resources table. Any additional information required to reanalyze the data reported in this paper is available from the lead contact upon reasonable request.

Methods references

60. Liu, J., Huang, J., Wei, X., Cheng, P. & Pu, K. Near-infrared chemiluminescence imaging of chemotherapy-induced peripheral neuropathy. *Adv. Mater.* **36**, 2310605 (2024).

61. Gnaim, S. & Shabat, D. Self-immolative chemiluminescence polymers: innate assimilation of chemiexcitation in a domino-like depolymerization. *J. Am. Chem. Soc.* **139**, 10002–10008 (2017).

62. Nakagawa, S. et al. A new blood–brain barrier model using primary rat brain endothelial cells, pericytes and astrocytes. *Neurochem. Int.* **54**, 253–263 (2009).

63. Butler, A., Hoffman, P., Smibert, P., Papalexi, E. & Satija, R. Integrating single-cell transcriptomic data across different conditions, technologies, and species. *Nat. Biotechnol.* **36**, 411–420 (2018).

64. McGinnis, C. S., Murrow, L. M. & Gartner, Z. J. DoubletFinder: doublet detection in single-cell RNA sequencing data using artificial nearest neighbors. *Cell Syst.* **8**, 329–337.e4 (2019).

65. Becht, E. et al. Dimensionality reduction for visualizing single-cell data using UMAP. *Nat. Biotechnol.* **37**, 38–44 (2019).

66. Korsunsky, I. et al. Fast, sensitive and accurate integration of single-cell data with Harmony. *Nat. Methods* **16**, 1289–1296 (2019).

67. Zhang, X. et al. CellMarker: a manually curated resource of cell markers in human and mouse. *Nucleic Acids Res.* **47**, D721–D728 (2019).

68. Wu, T. et al. clusterProfiler 4.0: a universal enrichment tool for interpreting omics data. *Innovation* **2**, 100141 (2021).

69. Cao, J. et al. Decoder-seq enhances mRNA capture efficiency in spatial RNA sequencing. *Nat. Biotechnol.* **42**, 1735–1746 (2024).

70. Hafemeister, C. & Satija, R. Normalization and variance stabilization of single-cell RNA-seq data using regularized negative binomial regression. *Genome Biol.* **20**, 296 (2019).

71. Pham, D. et al. Robust mapping of spatiotemporal trajectories and cell–cell interactions in healthy and diseased tissues. *Nat. Commun.* **14**, 7739 (2023).

72. Thompson, A. et al. Tandem mass tags: a novel quantification strategy for comparative analysis of complex protein mixtures by MS/MS. *Anal. Chem.* **75**, 1895–1904 (2003).

73. Cox, J. & Mann, M. MaxQuant enables high peptide identification rates, individualized p.p.b.-range mass accuracies and proteome-wide protein quantification. *Nat. Biotechnol.* **26**, 1367–1372 (2008).

74. Tyanova, S. et al. The Perseus computational platform for comprehensive analysis of (prote)omics data. *Nat. Methods* **13**, 731–740 (2016).

75. Szklarczyk, D. et al. The STRING database in 2023: protein–protein association networks and functional enrichment analyses for any sequenced genome of interest. *Nucleic Acids Res.* **51**, D638–D646 (2023).

76. Faul, F., Erdfelder, E., Lang, A.-G. & Buchner, A. G*Power 3: a flexible statistical power analysis program for the social, behavioral and biomedical sciences. *Behav. Res. Methods* **39**, 175–191 (2007).

Acknowledgments

We thank members of the Tian laboratory for helpful discussions and technical support, the Instrumental Analysis Center of East China Normal University for assistance with spectroscopy and microscopy experiments. We acknowledge Fudan University and Shanghai Jiao Tong University for providing access to imaging and behavioral platforms. We thank Dr. Chaoyong Yang for valuable advice on experimental design of omics studies. This work was supported by the National Natural Science Foundation of China (22393930 and 21811540027, 22404057 to Y. T.), the 2022 Shanghai "Science and Technology Innovation Action Plan" Fundamental Research Project (22JC1401200 to Y. T.), the Ministry of Science and Technology of China (2022YFA1106400 to Y. C.), the National Natural Science Foundation (82573109/82273304 to Y. C.), the National Key Research and Development Program of China (2024YFA0917700 to X. M.), the Natural Science Foundation (32325024 to X. M.) and the National Natural Science Foundation (22404059 to J. S.).

Author Contributions

Y. T., Y. C. and X. M. supervised the project. Y. T., Y. C., Y. D. and X. L. conceived the study and designed the experiments. Y. D. performed the experiments, data analysis and interpreted results. X. L. and M. G. performed the bioinformatics analyses. Z. L. assisted with data collection. Y. L. assisted with data visualization. Q. Z. supervised the immunofluorescence staining experiments. J. W. supervised the experimental design and data analysis of the proteomics study. Y. D., Y. T., Y. C. and X. L wrote the manuscript. J. S. helped improve the writing and designed the figures. Y. D., Y. T., Y. C, X. L, J. S. and Z. L. reviewed and approved the final version of the paper.

Competing interests

All authors declare no competing interests.

Additional information

Extended data

Supplementary information

Correspondence and requests for materials

Peer review information

Reprints and permissions information

Supplementary Files

This is a list of supplementary files associated with this preprint. Click to download.

- Supplementalinformation.docx